

Canted antiferromagnetic phases in the layered candidate Weyl material EuMnSb_2

J. M. Wilde,^{1,2} S. X. M. Riberolles,¹ Atreyee Das,^{1,2} Y. Liu,^{1,*} T. W. Heitmann,^{3,4} X. Wang,⁵ W. E. Straszheim,⁶ S. L. Bud'ko,^{1,2} P. C. Canfield,^{1,2} A. Kreyssig,^{1,2,†} R. J. McQueeney,^{1,2} D. H. Ryan,^{7,‡} and B. G. Ueland^{1,2,§}

¹Ames Laboratory, U.S. DOE, Iowa State University, Ames, Iowa 50011, USA

²Department of Physics and Astronomy, Iowa State University, Ames, Iowa 50011, USA

³University of Missouri Research Reactor, University of Missouri, Columbia, Missouri 65211, USA

⁴Department of Physics and Astronomy, University of Missouri, Columbia, Missouri 65211, USA

⁵Neutron Scattering Division, Oak Ridge National Laboratory, Oak Ridge, TN 37831, USA

⁶Materials Analysis and Research Laboratory, Office of Biotechnology, Iowa State University, Ames, Iowa 50011, USA

⁷Physics Department and Centre for the Physics of Materials,
McGill University, 3600 University Street, Montreal, Quebec, H3A 2T8, CA

(Dated: August 1, 2022)

EuMnSb_2 is a candidate topological material which can be tuned towards a Weyl semimetal, but there are differing reports for its antiferromagnetic (AFM) phases. The coupling of bands dominated by pure Sb layers hosting topological fermions to Mn and Eu magnetic states provides a potential path to tune the topological properties. Here we present single-crystal neutron diffraction, magnetization, and heat capacity data as well as polycrystalline ^{151}Eu Mössbauer data which show that three AFM phases exist as a function of temperature, and we present a detailed analysis of the magnetic structure in each phase. The Mn magnetic sublattice orders into a C-type AFM structure below $T_{\text{N}_{\text{Mn}}} = 323(1)$ K with the ordered Mn magnetic moment μ_{Mn} lying perpendicular to the layers. AFM ordering of the Eu sublattice occurs below $T_{\text{N}_{\text{Eu1}}} = 23(1)$ K with the ordered Eu magnetic moment μ_{Eu} canted away from the layer normal and μ_{Mn} retaining its higher temperature order. μ_{Eu} is ferromagnetically aligned within each Eu layer but exhibits a complicated AFM layer stacking. Both of these higher temperature phases are described by magnetic space group (MSG) $Pn'm'a'$ with the chemical and magnetic unit cells having the same dimensions. Cooling below $T_{\text{N}_{\text{Eu2}}} = 9(1)$ K reveals a third AFM phase where μ_{Mn} remains unchanged but μ_{Eu} develops an additional substantial in-plane canting. This phase has MSG $P11\frac{2_1}{a'}$. We also find some evidence of short-range magnetic correlations associated with the Eu between $12 \text{ K} \lesssim T \lesssim 30 \text{ K}$. Using the determined magnetic structures, we postulate the signs of nearest-neighbor intralayer and interlayer exchange constants and the magnetic anisotropy within a general Heisenberg-model. We then discuss implications of the various AFM states in EuMnSb_2 and their potential for tuning topological properties.

I. INTRODUCTION

Topological semimetals offer exotic physical properties such as chiral-charge pumping and linear-negative longitudinal magnetoresistance associated with relativistic Weyl fermions [1–5]. These properties arise from nontrivial topology of the bulk and surface electronic-band structures, which are intimately connected to the underlying symmetry of the crystal lattice and any magnetic order. Thus, modifying magnetic order can offer control of topological properties.

Relativistic (nearly massless) Dirac fermions generally occur in the linearly dispersing electronic bands forming Dirac cones [2–4]. Surface-Dirac cones with nodes at or near the Fermi energy E_{F} are of particular interest because they can give rise to topologically induced transport properties [1, 5]. Further, topological materials with a net magnetization M that can be readily tuned by temperature or external fields are especially sought after because they can offer direct control of Dirac surface states [4]. For example, the presence of a net

M in a topological-crystalline insulator can result in the gapping of a surface-Dirac cone: gapless surface-Dirac cones are associated with chiral-locked dissipationless surface conductivity or edge states whereas gapped surface-Dirac cones lead to quantum-anomalous-Hall type conductivity [6].

The emergence of certain magnetic order or application of a strong enough magnetic field H can lift the spin degeneracy of the bulk-Dirac cones in a semimetal [7]. This creates two Weyl nodes for each Dirac node and the associated relativistic Weyl fermions. The two Weyl nodes have opposite chirality (i.e. + or – chirality) and can be viewed as chiral monopoles (sources and sinks of Berry curvature) connected by surface Fermi arcs. An unequal number of + or – chiral charges created through, for example, the application of parallel electric and magnetic fields results in the chiral anomaly which gives rise to important topologically induced properties such as linear-negative-longitudinal magnetoresistance [5].

Examples of Weyl semimetals (WSMs) have been observed for crystals with broken inversion symmetry \mathcal{I} (e.g. TaAs [8] and NbAs [9]). However, very few examples of materials with broken time-reversal symmetry \mathcal{T} exist, and magnetic ordering offers a way to break \mathcal{T} . Searches for such broken \mathcal{T} WSMs have included AMnX_2 , $A = \text{Ca, Sr, Ba, Yb, or Eu}$ and $X = \text{Sb or Bi}$, with magnetic moments due to the Mn and Eu and highly anisotropic Dirac cones within the Sb and Bi square or zig-zag nets [10–12]. As compared to tetragonal 112 compounds, the orthorhombic variants with $A = \text{Eu}$,

* Present Address: Crystal Growth Facility, Institute of Physics, École Polytechnique Fédérale de Lausanne, CH-1015 Lausanne, CH

† Present Address: Ruhr-Universität Bochum, Universitätsstraße 150 44801 Bochum, DE

‡ dominic@physics.mcgill.ca

§ bgueland@ameslab.gov, bgueland@gmail.com

Yb, and Sr are particularly interesting because ferromagnetic (FM) canting of the ordered magnetic moment μ can occur without further reduction of the underlying chemical symmetry. Such canting can lift the degeneracy of the Dirac cones to form Weyl nodes.

EuMnSb₂ is a particularly compelling candidate Weyl semimetal because it contains two magnetic species and the slightly orthorhombic unit cell permits the existence of a net M canted away from the layer normal without the magnetic domain formation required for the tetragonal 112s. Figure 1 shows the orthorhombic chemical-unit cell for EuMnSb₂ which has space group $Pnma$ and lattice parameters of $a = 22.4958(1)$ Å, $b = 4.3758(1)$ Å, and $c = 4.3908(1)$ Å at a temperature of $T = 50$ K. Such $AMnX_2$ compounds generally contain repeating $A-X1-Mn-X1-A$ blocks along a that are separated by $X2$ layers hosting topological fermions. Here, $X1$ and $X2$ denote X ions on different crystallographic sites. For the orthorhombic unit cell, the $X2$ layers are not square, as found in the tetragonal 112s, but are made up of the zig-zag chains shown in Fig. 1(b).

The occurrence of both topological fermions and magnetic ions provides a potential path to tune the topological properties via magnetic order. Indeed, Hall resistivity data for antiferromagnetic (AFM) EuMnBi₂ show the occurrence of the half-integer-quantum-Hall effect where control of the Eu magnetic sublattice via a magnetic field is reported to suppress the interlayer coupling between Bi layers hosting Dirac fermions [14]. For EuMnSb₂, angle-resolved-photoemission-spectroscopy (ARPES) data show Dirac like linear dispersion near E_F , and magnetotransport data indicate that exchange induced effects of the Eu magnetism affect the electronic transport [15].

The magnetic ordering of EuMnSb₂ has been previously studied by neutron diffraction using both powder [15] and single-crystal samples [16, 17], however, Ref. 17 reports a tetragonal rather than orthorhombic chemical-unit cell. All three studies find two AFM transitions, one at a Néel temperature of $T_{N_{Mn}} = 350(2)$ K [15] ($T_{N_{Mn}} \approx 346$ K [16], $T_{N_{Mn}} \approx 340$ K [17]) due to ordering of the Mn and one at a Néel temperature of $T_{N_{Eu}} = 21(1)$ K [15] ($T_{N_{Eu}} \approx 21$ K [16], $T_{N_{Eu}} \approx 22$ K [17]) owing to ordering of the Eu. For the Mn AFM order the studies find the C-type magnetic structure shown in Fig. 1(e), with neighboring Mn spins within a layer being antiferromagnetically oriented and FM alignment of neighboring Mn spins along the direction perpendicular to the Sb layers. The studies concluded that the ordered Mn magnetic moment μ_{Mn} lies perpendicular to the Sb layers, and that the Mn sublattice retains this magnetic structure upon cooling through $T_{N_{Eu}}$ [15, 16]. Resistivity versus temperature data show a maximum at $T_{N_{Eu}}$ and either metallic [15] or semiconducting [18] behavior below $T_{N_{Eu}}$.

The results from the powder [15] and single-crystal [16, 17] neutron diffraction studies differently describe the magnetic structure of the Eu sublattice below $T_{N_{Eu}}$. The powder study finds A-type AFM order with FM Eu layers stacked antiferromagnetically along a and an ordered Eu magnetic moment μ_{Eu} lying along c [15]. Ref. 16 finds a canted AFM structure with μ_{Eu} lying in the ac plane. The structure consists of

FM Eu layers with a staggered a component of μ_{Eu} in neighboring layers. The relative orientation of the c component of μ_{Eu} has a $\rightarrow\leftarrow\leftarrow\leftarrow$ pattern along a , as shown in Fig. 1(f). Ref. 17 finds an AFM structure with a $\leftarrow\rightarrow\rightarrow\leftarrow$ pattern along c , but μ_{Eu} lying solely along a . Note that in the tetragonal setting of Ref. 17 c is perpendicular to the Eu, Sb1-Mn-Sb1, and Sb2 layers. There is zero M associated with the determined orders, and Ref. 16 found that $\mu_{Mn} = 4.5(6) \mu_B$ and $\mu_{Eu} = 5.9(8) \mu_B$ at $T = 7$ K. Ref. 17 reports $\mu_{Mn} = 4.6(2) \mu_B$ and $\mu_{Eu} = 5.2(4) \mu_B$ at 5 K. Notably, the value of μ_{Eu} is less than the expected value of $7 \mu_B$ for Eu^{2+} .

Here, we report magnetization, heat capacity, ¹⁵¹Eu Mössbauer spectroscopy, and single-crystal neutron diffraction results for EuMnSb₂. Our data are consistent with a canted AFM phase below $T_{N_{Eu}}$ and we present results showing a third AFM phase occurring below $T_{N_{Eu2}} = 9(1)$ K. Our detailed single-crystal neutron diffraction study has determined the magnetic structure in each of the three AFM phases, which are shown in Figs. 1(e)–1(g). Based on these results, we postulate the sign of nearest-neighbor (NN) exchange interactions and magnetic anisotropy for a generic Heisenberg model and make comparisons with EuMnBi₂ and SrMnSb₂, as well as other reports for EuMnSb₂. We also discuss the possible influences of disorder, the geometric arrangement of ions in the $X2$ layers, and the magnetic order on the topological properties.

II. EXPERIMENT

Plate-like single crystals of EuMnSb₂ were flux grown and screened by x-ray diffraction. The growth of EuMnSb₂ single crystals is similar to the growth of SrMnSb₂ single crystals described in detail in Ref. [12]. Europium pieces, manganese powder, and antimony chunks were weighed at a molar ratio of Eu:Mn:Sb = 1:1:10 and loaded into an alumina crucible in a glovebox with an argon atmosphere. The alumina crucible was sealed in an evacuated quartz tube with a backfilling of 300 mbar of argon gas and then heated up to $T = 1273$ K. After a dwell time of 12 hours, the tube was slowly cooled to 873 K at a rate of 3 K/h. Plate-like single crystals with masses of $m \lesssim 40$ mg were cleaved from the matrix. X-ray diffraction data for ground single crystals were consistent with previous results for the chemical-unit cell although significant texture induced effects in the diffraction pattern prevented accurate determination of the stoichiometry. The composition of single crystals of EuMnSb₂ were quantitatively determined by Energy-Dispersive Spectroscopy (EDS) as described in Sec. III A.

Magnetization measurements were made down to $T = 1.8$ K and up to $\mu_0 H = 7$ T using a Quantum Design, Inc., Magnetic Property Measurement System with a superconducting quantum interference device. Measurements of the heat capacity at constant pressure C_p were made down to 1.8 K in a Quantum Design, Inc., Physical Property Measurement System using a standard semi-adiabatic heat-pulse technique.

¹⁵¹Eu Mössbauer spectroscopy measurements were carried

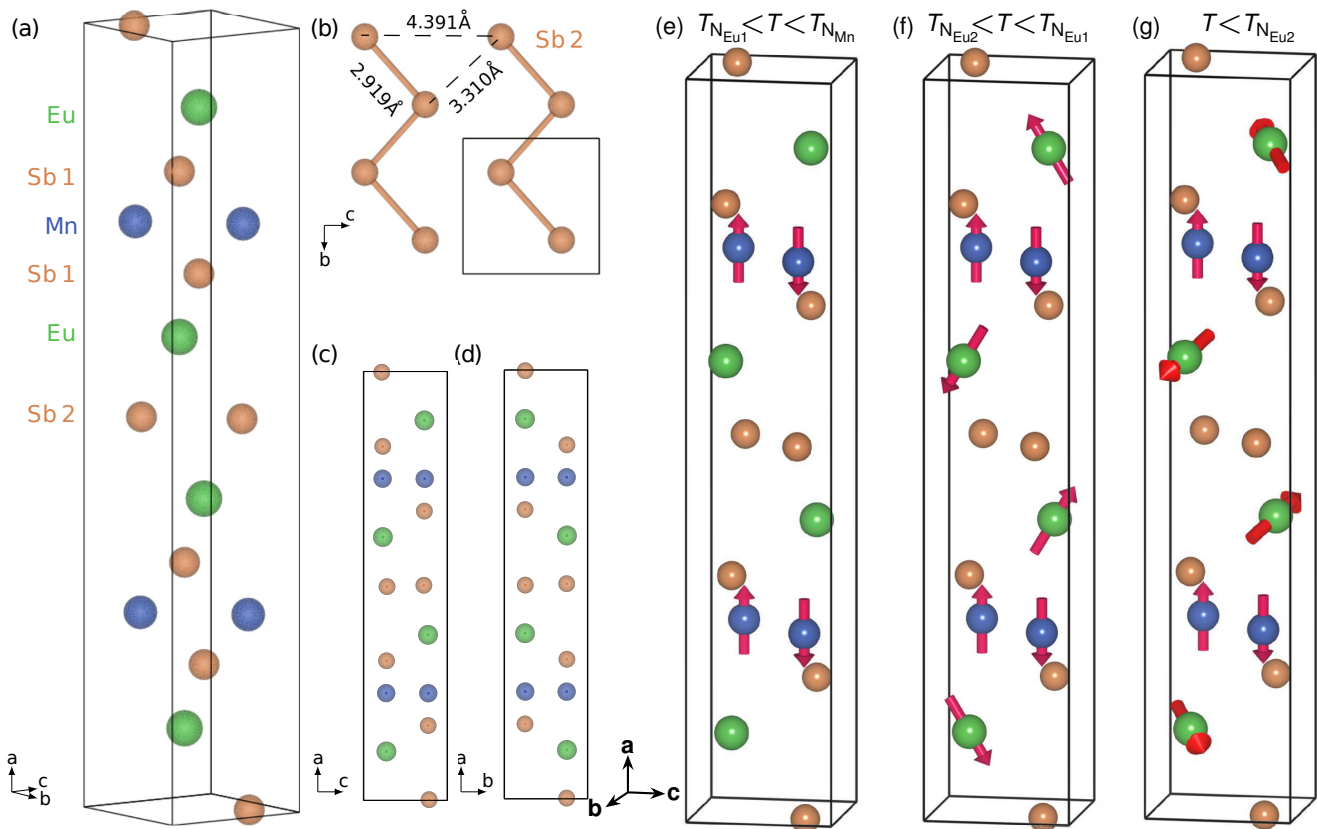


FIG. 1. (a) The chemical structure of EuMnSb_2 with $a = 22.4958 \text{ \AA}$, $b = 4.3758 \text{ \AA}$, and $c = 4.3908 \text{ \AA}$. The orthorhombic unit cell is drawn with gray lines, and the two Sb sites are labeled Sb 1 and Sb 2. (b) The Sb 2 layer as viewed by looking down the a axis. (c),(d) Views of the chemical unit cell looking down b (c) and up c (d). (e), (f), and (g) show the antiferromagnetic order occurring at temperatures of $T_{\text{NEu1}} < T < T_{\text{NMn}}$, $T_{\text{NEu2}} < T < T_{\text{NEu1}}$, and $T < T_{\text{NEu2}}$, respectively, where $T_{\text{NMn}} = 323(1) \text{ K}$, $T_{\text{NEu1}} = 23(1) \text{ K}$, and $T_{\text{NEu2}} = 9(1) \text{ K}$. These diagrams were made using VESTA [13].

out using a 4 GBq $^{151}\text{SmF}_3$ source driven in sine mode and calibrated using a standard $^{57}\text{CoRh}/\alpha\text{-Fe}$ foil. Isomer shifts are quoted relative to EuF_3 at ambient temperature. The sample consisted of ground single crystals and was cooled in a vibration-isolated-closed-cycle-He refrigerator with the sample in He exchange gas. The hyperfine spectra were fitted at each temperature to a sum of Lorentzian lineshapes. The intensities and positions of the lines were derived from a full solution to the nuclear Hamiltonian [19]. Spectra taken above $T = 10 \text{ K}$ were also fitted using a model that derives a distribution of hyperfine fields by assuming an incommensurate magnetic structure with a sinusoidally modulated value for μ [20, 21].

Single-crystal neutron diffraction measurements were made on the TRIAX triple-axis-neutron spectrometer at the University of Missouri Research Reactor and on the TOPAZ diffractometer at the Spallation Neutron Source, Oak Ridge National Laboratory. Measurements on TRIAX were made using a neutron wavelength of $\lambda = 1.638 \text{ \AA}$ selected by a pyrolytic-graphite (PG) monochromator. A PG analyzer was employed to reduce background scattering. Söller-slit collimators with divergences of $60'-60'-80'-80'$ were inserted be-

fore the monochromator, between the monochromator and sample, between the sample and analyzer, and between the analyzer and detector, respectively. Higher resolution measurements were made using $60'-60'-20'-20'$ Söller-slit collimators. PG filters were inserted before and after the sample to reduce contamination by higher order neutron wavelengths.

On TRIAX, the sample was mounted to an Al holder and placed inside of an Al can. The can was filled with He exchange gas, sealed, and attached to the cold head of a closed-cycle-He refrigerator which allowed for measurements between $T = 6$ and 340 K . As explained below, crystal twinning permitted the simultaneous collection of data for both the $(hk0)$ and $(h0l)$ scattering planes, where h , k , and l are Miller indices. Corrections for neutron absorption were performed with MAG2POL [22].

TOPAZ is a time-of-flight neutron diffractometer which utilizes the wavelength-resolved-Laue-diffraction technique [23]. The same single-crystal sample used for the TRIAX experiments was connected to an Al holder and attached to the instrument's cryogenic goniometer which allowed for cooling down to $T = 5 \text{ K}$. Measurements were made at 5, 12, and 50 K for various orientations of the crystal with the $(h0l)$

plane horizontal. Twinning was also observed during this experiment and allowed for the observation of peaks in the $(h k 0)$ plane. Corrections for neutron absorption were performed using ANVRED [24] and data were analyzed using single-crystal refinements done with JANA [25].

III. RESULTS

A. Energy Dispersive Spectroscopy

EDS measurements were made using an Oxford Instruments Aztec EDS x-ray analyzer with an X-Max-80 detector mounted on an FEI Quanta-FEG scanning electron microscope. Samples were measured using a voltage of 15 kV and a current of ≈ 0.8 nA. Spectra were collected for 30 s at 19000 counts per s. The Eu L line series was used to quantify the amount of Eu with reference to a vitreous Eu standard. The Mn K line series and the Sb L line series were used with reference to pure element standards. All standards were internal to the Oxford software. Several other reference materials, e.g. Eu phosphate, were used to establish the accuracy of the results.

The average from 11 spot measurements spanning 2 different areas of a single crystal yielded ratios of Mn/Sb = 0.49(1), Eu/Sb = 0.51(1), and Eu/Mn = 1.04(2) for the stoichiometry. The measurement precision for the Eu content is 1 part out of 79 (1.3%).

B. Magnetization and Heat Capacity

Figure 2(a) shows $M/\mu_0 H$ versus temperature for $\mu_0 H = 0.1$ T for $\mathbf{H} \parallel \mathbf{a}$ and $\mathbf{H} \perp \mathbf{a}$. Changes in the slopes of the curves are evident for both field directions at $T \approx 23$ and 9 K which correspond to the AFM transitions at $T_{N_{Eu1}}$ and $T_{N_{Eu2}}$, respectively. We show below via our neutron diffraction results that the magnetic ordering of the Mn sublattice does not change upon crossing $T_{N_{Eu1}}$ and $T_{N_{Eu2}}$, with μ_{Mn} lying along \mathbf{a} for $T < T_{N_{Mn}}$. Rather, the two transition temperatures are associated with a paramagnetic (PM) to AFM transition for the Eu sublattice ($T_{N_{Eu1}}$) and a change in the AFM structure of the Eu sublattice ($T_{N_{Eu2}}$). With these facts in mind, examining the region between $T_{N_{Eu1}}$ and $T_{N_{Eu2}}$, we see that $M/\mu_0 H$ for $\mathbf{H} \parallel \mathbf{a}$ decreases with decreasing T whereas $M/\mu_0 H$ for $\mathbf{H} \perp \mathbf{a}$ gently increases. For a typical AFM, these data would suggest that the ordered magnetic moment lies primarily along \mathbf{a} . The data for $T < T_{N_{Eu2}}$, on the other hand, suggest that the ordered moment has a significant component perpendicular to \mathbf{a} . This is consistent with the AFM structures we report below where we find from neutron diffraction that μ_{Eu} has its largest component lying along \mathbf{a} for $T_{N_{Eu1}} > T > T_{N_{Eu2}}$ but its largest component lies perpendicular to \mathbf{a} for $T < T_{N_{Eu2}}$.

Figure 2(b) shows $M(H)$ at $T = 1.8$ K for $\mathbf{H} \parallel \mathbf{a}$ and $\mathbf{H} \perp \mathbf{a}$. Both curves increase with increasing H and show no signs of magnetic saturation up to $\mu_0 H = 7$ T. The curves are similar to those previously reported [16], with the $\mathbf{H} \perp \mathbf{a}$

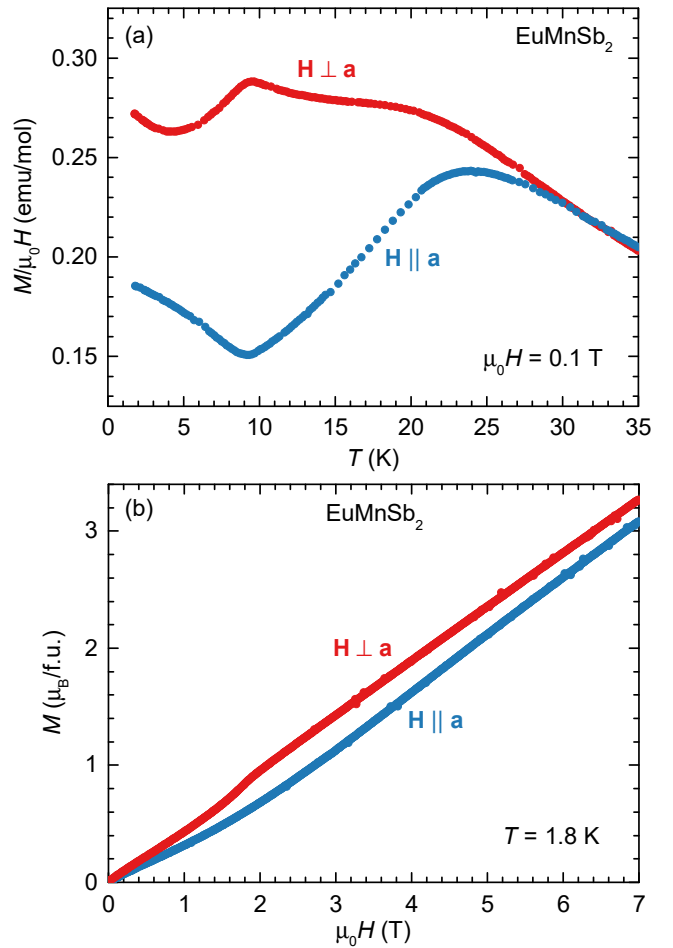


FIG. 2. (a) The magnetization divided by magnetic field versus temperature for \mathbf{H} applied parallel or perpendicular to \mathbf{a} . (b) The magnetization versus magnetic field at $T = 1.8$ K for \mathbf{H} applied parallel or perpendicular to \mathbf{a} . f.u. stands for formula unit.

curve lying above the $\mathbf{H} \parallel \mathbf{a}$ curve and the two curves adopting linear behavior above ≈ 2 T. Both show a change in slope beginning at ≈ 1.5 T. For $\mathbf{H} \parallel \mathbf{a}$, the deviation may be associated with gradual rotation of μ_{Eu} towards \mathbf{a} because, as we show below, μ_{Mn} lays only along \mathbf{a} whereas μ_{Eu} has components along all three crystallographic directions. One might expect a spin-flop of the Mn spins for $\mathbf{H} \parallel \mathbf{a}$ if μ_{Mn} were reorienting and a previous report shows a step-like feature in $M(H)$ data at 2 K for $\mathbf{H} \parallel \mathbf{a}$ which is attributed to a spin flop occurring at 1.5 T [18]. On the other hand, similar to our data in Fig. 2(b), data in Ref. [16] do not show a clear-cut indication for a spin flop. For $\mathbf{H} \perp \mathbf{a}$, the change in slope near 1.5 T may represent both μ_{Eu} and μ_{Mn} reorienting towards \mathbf{H} .

Figure 3 shows C_p/T versus T data and the inset shows $C_p(T)$. Two peaks are observed: one broad peak corresponding to $T_{N_{Eu1}}$ and a weaker peak associated with $T_{N_{Eu2}}$. Taken together with the features observed in $[M/\mu_0 H](T)$, the peaks in $[C_p/T](T)$ indicate a change in entropy S due to magnetic phase transitions at $T_{N_{Eu1}}$ and $T_{N_{Eu2}}$. Our $[C_p/T](T)$ data spanning $T_{N_{Eu1}}$ are consistent with the broadness and the size of the

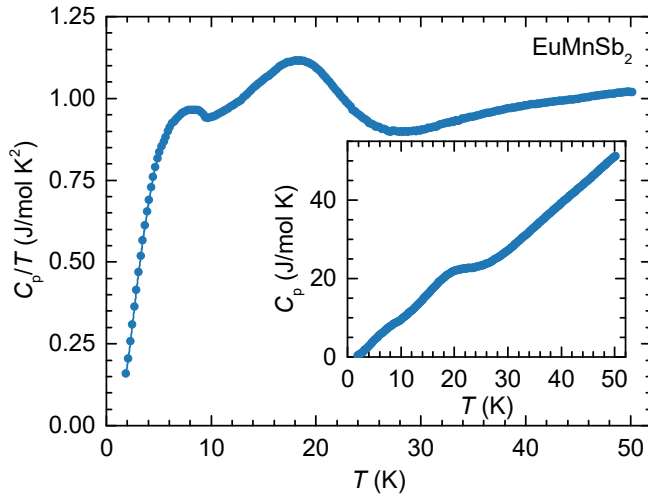


FIG. 3. The isobaric heat capacity divided by temperature versus temperature. The inset shows the isobaric heat capacity versus temperature.

peak shown in Ref. [18], which reports an estimated change in the magnetic component of S of $\approx 80\%$ of the value of $S_{\text{Eu}} = 17.3 \text{ J/mol-K}$ expected for $S = 7/2 \text{ Eu}^{2+}$. A less pronounced peak at $T_{\text{N}_{\text{Eu}2}}$ is seen in Ref. [18], and we estimate that the small peak at $T_{\text{N}_{\text{Eu}2}}$ in our $[C_p/T](T)$ data would contribute only an additional $S \approx 0.1 \text{ J/mol-K}$. Nevertheless, the data we present below clearly indicate that the Eu sublattice undergoes successive magnetic transitions at temperatures corresponding to the peaks in $C_p(T)$.

AFM transitions typically are expected to yield much sharper peaks in $C_p(T)$ than those shown in Fig. 3. Broadening of these peaks could be due to disorder not detected by our EDS and x-ray measurements. However, as we discuss below, the ^{151}Eu Mössbauer spectroscopy and neutron diffraction data show evidence for short-range magnetic correlations associated with the Eu sublattice which can also broaden the peaks in $C_p(T)$.

C. ^{151}Eu Mössbauer spectroscopy

The ^{151}Eu Mössbauer spectrum of EuMnSb_2 at $T = 5 \text{ K}$ shown in Fig. 4(a) is typical of a magnetically ordered Eu^{2+} compound. There is a sharp, well-split magnetic pattern with a hyperfine field of $B_{\text{hf}} = 27.0(1) \text{ T}$ and an isomer shift of $-11.4(1) \text{ mm/s}$. In addition there is a small [4(1)%] contribution from a Eu^{3+} impurity with an isomer shift of $+0.7(1) \text{ mm/s}$. The impurity was either introduced during handling of the sample or is associated with residual flux from the growth process. This component is more apparent at higher temperatures [e.g. at 50 K in Fig. 4(a)]. It is not magnetic and does not affect the fitting. The evolution of the spectra on warming is not typical of a simple AFM \rightarrow PM transition: above 12.5 K the lines clearly broaden, and the spectra develop increased weight towards the center of the pattern, reflecting the growing presence of a distribution of

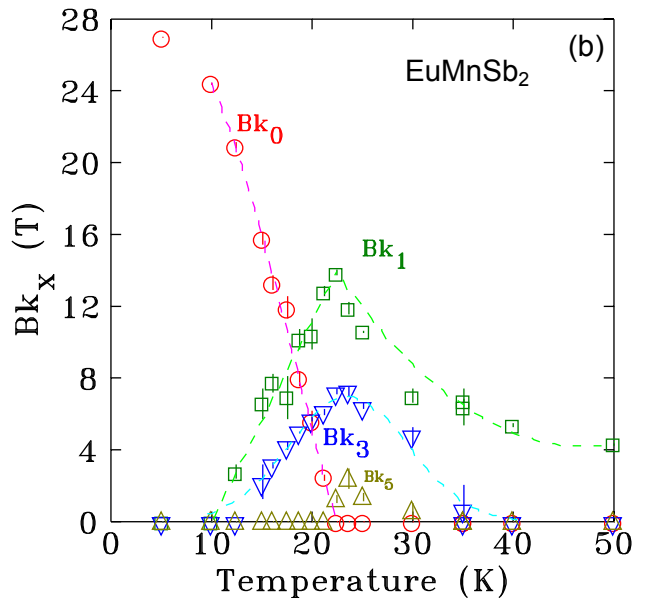
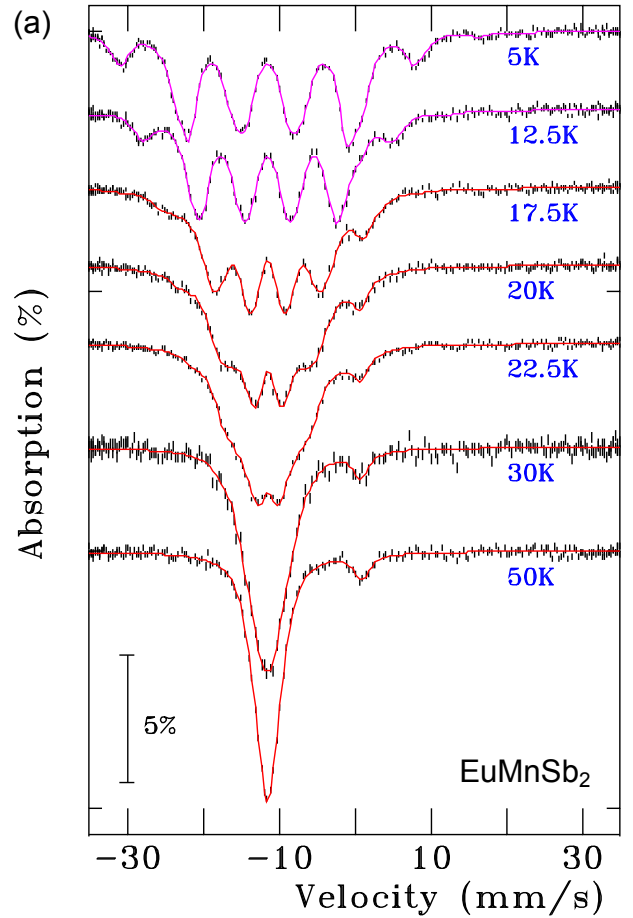


FIG. 4. (a) ^{151}Eu Mössbauer spectra of EuMnSb_2 at various temperatures. Solid lines are fits using the two models described in the text: Magenta lines – full Hamiltonian, used for $T = 5$ and 12.5 K ; red lines – incommensurate modulation. (b) Amplitudes of the Fourier components (Bk_x) used to fit the modulated structure, as described in the text.

hyperfine fields.

We found that the spectra above $T = 10$ K are best fitted by assuming a model in which the Eu moments (and, by extension, B_{hf}) develop an incommensurate modulated structure on warming. Following Bonville et al. [20] and Maurya et al. [21], we denote the AFM propagation vector as \mathbf{k} in this subsection instead of $\boldsymbol{\tau}$, and assume that the modulation in μ along \mathbf{k} can be written in terms of its Fourier components and that B_{hf} is a linear function of μ at any given site. Then the variation of B_{hf} with distance x along \mathbf{k} can be written as [20]

$$B_{\text{hf}}(kx) = Bk_0 + \sum_{l=0}^n Bk_{2l+1} \sin[(2l+1)kx]. \quad (1)$$

Bk_n are the odd Fourier coefficients of the field modulation and kx is a position in reciprocal space along the direction of \mathbf{k} . As $+B_{\text{hf}}$ and $-B_{\text{hf}}$ are indistinguishable, kx only needs to run over half of the modulation period. Variations of this modeling have been used to fit spectra for EuPdSb [20], Eu_4PdMg [26], $\text{Eu}(\text{Co}_{1-x}\text{Ni}_x)_{2-y}\text{As}_2$ [27], and EuIn_2As_2 [6].

Figure 4(b) shows the evolution of the fitted Fourier components. As the constant term Bk_0 falls with increasing T , the fundamental term Bk_1 and third harmonic term Bk_3 develop and rapidly dominate the fits as the distribution of B_{hf} becomes broader. By $T \approx 22$ K Bk_0 is gone, and only the modulated components remain. The broadening of B_{hf} appears to persist past 250 K. However, the patterns are not well enough resolved to assign a meaningful form to the distribution, but the feature associated with Eu^{2+} continues to sharpen on warming. This residual contribution to B_{hf} is likely due to short-range magnetic correlations of the Eu. The neutron diffraction data presented below find evidence for such correlations above $T_{\text{N}_{\text{Eu1}}}$.

Figure 5 shows the temperature dependence of B_{hf} derived from the two models. The larger black circles show $\langle B_{\text{hf}} \rangle$ derived from the simple one-site full Hamiltonian model showing relatively conventional behaviour (other than the line broadening) up to $T = 20$ K that can be fitted to the expected $J = \frac{7}{2}$ Brillouin function for Eu^{2+} yielding an extrapolated magnetic transition temperature of 22.8(1) K. The average hyperfine field derived from the modulated fits (smaller cyan squares) tracks $\langle B_{\text{hf}} \rangle$ very well, showing that the two models are consistent. The moment modulation develops between 10 K and 12.5 K and Bk_0 (shown as the blue squares) falls away from $\langle B_{\text{hf}} \rangle$ quite rapidly. A simple linear fit yields an endpoint of 22.5(1) K, consistent with the extrapolation of $\langle B_{\text{hf}} \rangle$.

The ^{151}Eu Mössbauer analysis therefore suggests the presence of two magnetic events associated with the Eu sublattice: initial ordering into an incommensurate structure at $T \approx 22$ K that progressively squares up on cooling. The process completes just below 12.5 K. On the other hand, as shown below, our single-crystal neutron diffraction data show a commensurate AFM propagation vector below both $T_{\text{N}_{\text{Eu1}}}$ and $T_{\text{N}_{\text{Eu2}}}$. Thus, the incommensurate AFM Eu order between $T_{\text{N}_{\text{Eu2}}} \lesssim T < T_{\text{N}_{\text{Eu1}}}$ deduced from Mössbauer appears at odds with the commensurate AFM order seen by neutron diffraction. However, Mössbauer data for other Eu intermetallics in-

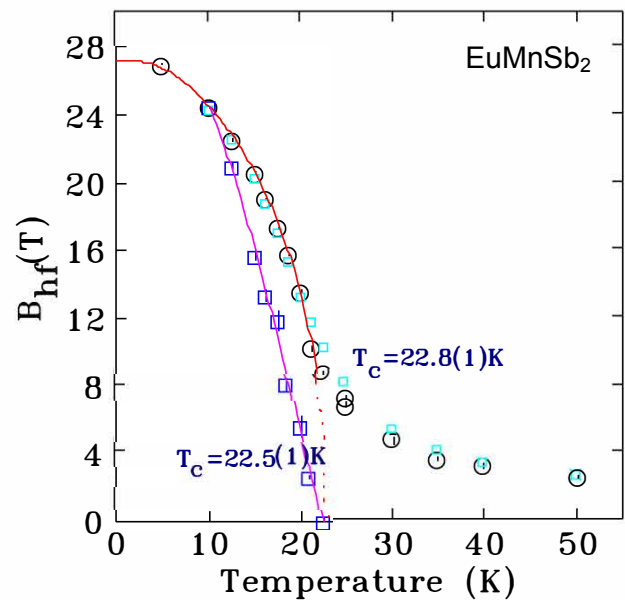


FIG. 5. Temperature dependence of the hyperfine field for EuMnSb_2 derived from the two models used to fit the spectra showing evidence for two transitions. The black circles show B_{hf} derived from a full Hamiltonian fit and represents an average that does not take account of any distribution. The solid red line is a $J = \frac{7}{2}$ Brillouin function, expected for Eu^{2+} and yielding an extrapolated transition temperature of $\approx 22.8(1)$ K. The small cyan squares show the average hyperfine field $\langle B_{\text{hf}} \rangle$ derived from the modulated model. The larger blue squares show the behavior of Bk_0 , the constant term in the Fourier expansion, which breaks away from $\langle B_{\text{hf}} \rangle$ above 10 K and reaches zero at 22.5(1) K. The residual contributions seen above 25 K are likely due to short-range magnetic correlations in the Eu sublattice.

dicating a commensurate AFM ground state and an incommensurate AFM propagation vector that develops as T approaches T_{N} [20, 21, 27]. It has been suggested that the development of the incommensurate propagation vector is tied to the presence of short-range magnetic correlations which persist even for $T < T_{\text{N}}$, although they eventually disappear with decreasing T [27]. As we show below, evidence for short-range magnetic correlations is found in our neutron diffraction data for $T \gtrsim T_{\text{N}_{\text{Eu1}}}$ which provides consistency between the neutron and Mössbauer results.

D. Single-Crystal Neutron Diffraction

The three ions in EuMnSb_2 are all located at the $4c$ Wyckoff position of space group $Pnma$ which does not have any special reflection conditions. Thus, only the general reflection conditions apply for the appearance of structural-Bragg peaks. These are: $(0kl)$ with $k+l = 2n$, $(h k 0)$ with $h = 2n$, $(h 0 0)$ with $h = 2n$, $(0 k 0)$ with $k = 2n$, and $(0 0 l)$ with $l = 2n$, where n is an integer. Bragg peaks observed at other positions may be due to magnetic ordering. Writing $Pnma$ in its unabbreviated form of $P \frac{2_1}{n} \frac{2_1}{m} \frac{2_1}{a}$ is helpful for understanding the data analysis.

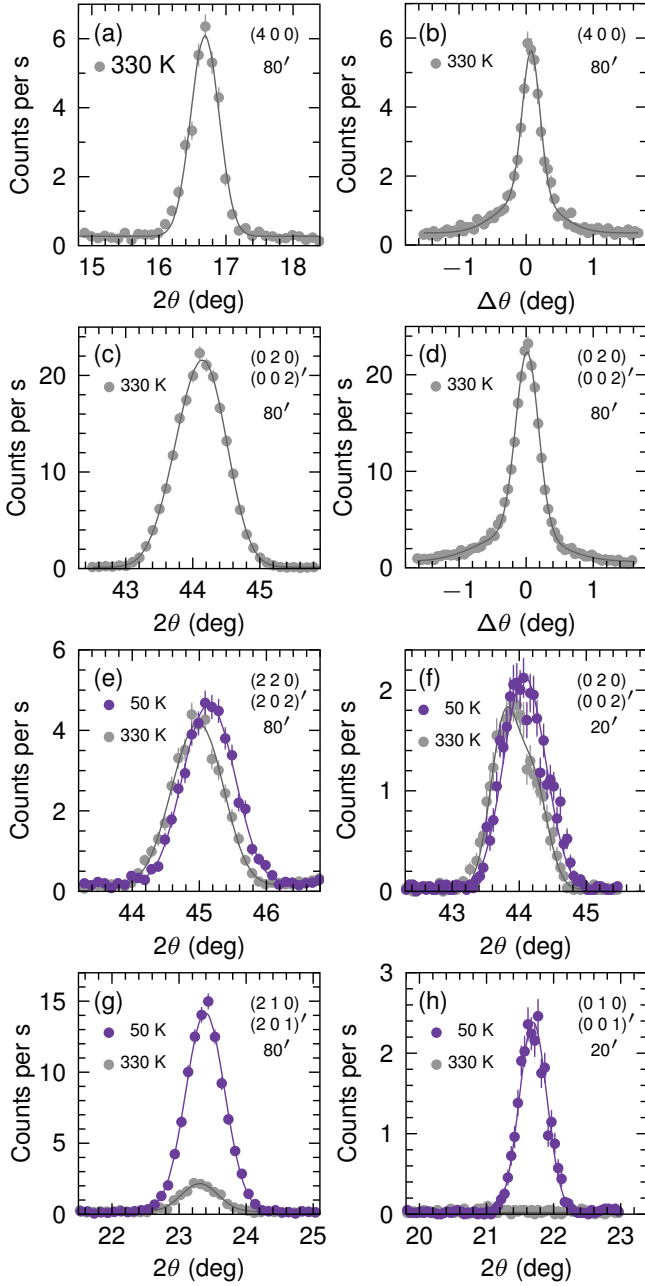


FIG. 6. Diffraction data for EuMnSb_2 from longitudinal (θ - 2θ) and rocking ($\Delta\theta$) scans made at various temperatures using a neutron wavelength of 1.638 Å. The label 80' (20') corresponds to 80' (20') Söller-slit collimators being used after the sample. Lines are fits as discussed in the text. [(a), (c)] θ - 2θ scan and [(b), (d)] rocking scan data for (400) [(a),(b)] and (020)/(002)' [(c),(d)] at $T = 330$ K. [(e), (g)] θ - 2θ scan data for (220)/(202)' (e) and (210)/(201)' (g) taken at 330 and 50 K. [(f), (h)] θ - 2θ scan data for (020)/(002)' (f) and (010)/(001)' (h) at 330 and 50 K using the tighter collimation.

Refinements to the single-crystal diffraction data taken on TOPAZ confirmed that $P_{\frac{21}{n} \frac{21}{m} \frac{21}{a}}$ correctly describes the chemical-unit cell. Goodness-of-fit and other parameters determined from the single-crystal refinements used to simul-

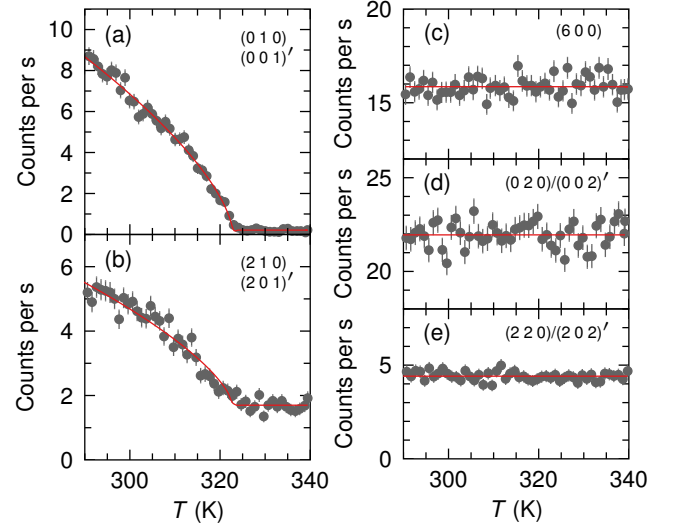


FIG. 7. Heights of the (010)/(001)' (a), (210)/(201)' (b), (600) (c), (020)/(002)' (d), and (220)/(202)' (e) Bragg peaks for EuMnSb_2 as functions of temperature. Lines in (a) and (b) are fits to $y_0 + (T_N - T)^{2\beta}$ where y_0 is a constant, T_N is the Néel temperature, and β is the critical exponent for the magnetic order parameter. The fits give $\beta \approx 0.3$. Lines in (c)–(e) are guides to the eye.

taneously determine the nuclear and magnetic structures are quoted at the end of Section III D in Table III. Refinements for the nuclear structure allowed the isotropic thermal factor U_{iso} and the atomic positions within the unit cell (x , y , and z) to vary. We were unable to get reliable and sensible results when allowing the occupancy of the sites to vary, and, therefore, assumed the sample to be stoichiometric, as found from EDS. The values of U_{iso} , x , y , z , and the twin populations determined at $T = 50$ K were used for the refinements made for the 12 and 5 K data.

Figures 6(a) and 6(b) show data from longitudinal (θ - 2θ) and transverse (rocking) scans, respectively, made across the (400) structural-Bragg peak at $T = 330$ K with 80' collimators after the sample. Similar data for (020)/(002)' are given in Figs. 6(c) and 6(d), where as we explain further below, these data contain contributions from two domains due to twinning. The Miller indices for the twin domain are labeled by a ' symbol. For both (400) and (020)/(002)', the longitudinal-scan data show single resolution-limited peaks centered at the expected positions which are well fit by a gaussian lineshape. The rocking-scan data, on the other hand, require fitting two gaussian peaks to fully account for the lineshape: a sharp resolution-limited peak accounting for the majority of the integrated intensity and a slightly broader, much weaker peak centered at a slightly lower rocking angle. This mosaic indicates the presence of two grains or for (020)/(002)' it could correspond to the tail of the Bragg peak from the twin.

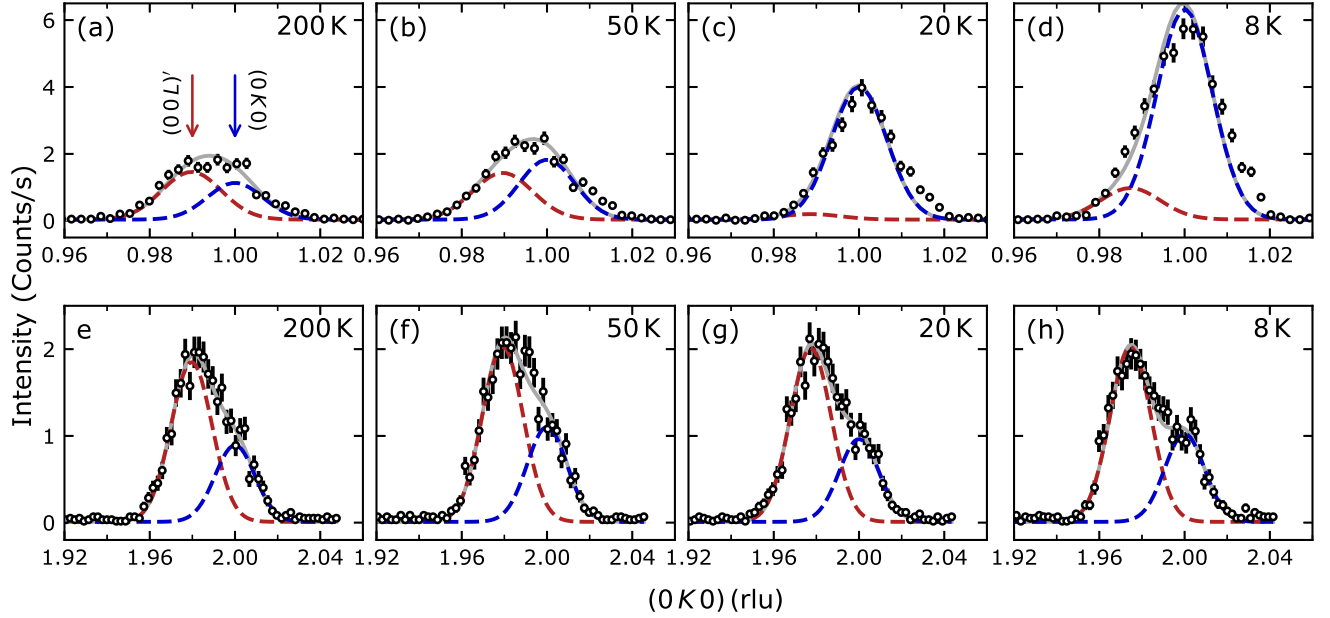


FIG. 8. Diffraction data for EuMnSb_2 for $(010)/(001)'$ (a-d) and $(020)/(002)'$ (e-h) from longitudinal (θ - 2θ) scans made at $T = 200$ K (a, e), $T = 50$ K (b, f), $T = 20$ K (c, g) and, $T = 8$ K (d, h) using $20'$ Söller-slit collimators after the sample. Data are plotted as a function of reciprocal lattice units (rlu) for the twinned directions $(0k0)$ and $(00l)'$. Gray lines show the two-gaussian fits to the data described in the text and red and blue dashed lines show the single-gaussian lineshapes for each twin. The slight shoulder in (b)–(d) above the fitted lineshape shows no substantial temperature dependence and does not affect the analysis presented in the text.

1. $T_{N_{Mn}} > T > T_{N_{Eu}}$

Data in Figs. 6(g), 6(h), 7(a) and 7(b) demonstrate that magnetic-Bragg peaks emerge upon cooling below $T_{N_{Mn}} = 323(1)$ K at $(210)/(201)'$ and $(010)/(001)'$. The $(210)/(201)'$ magnetic-Bragg peak occurs at the same position as a structural-Bragg peak whereas a structural-Bragg peak does not occur at $(010)/(001)'$. Magnetic-Bragg peaks at these positions highlight the need to consider twinning of the crystal which can result in misidentifying the Miller indices of a magnetic-Bragg peak. We were able to resolve both twin domains by inserting $20'$ collimators after the sample. This allowed us to simultaneously resolve $(hk0)$ and $(h0l)'$ Bragg peaks, but significantly increased the counting time.

Figures 8(a)–8(d) show data from longitudinal scans across the (010) and $(001)'$ magnetic-Bragg peak positions at $T = 200, 50, 20,$ and 8 K, respectively, using $20'$ collimators after the sample. The recorded lineshapes consists of two peaks, where the solid line is a fit to two gaussian peaks and the dashed lines show the (010) and $(001)'$ peaks in blue and red, respectively. Figures 8(e)–8(h) show similar data for the (020) and $(002)'$ structural-Bragg peaks. Since the (010) and $(001)'$ magnetic-Bragg peaks occur at smaller momentum transfers Q than the (020) and $(002)'$ structural-Bragg peaks, the individual (010) and $(001)'$ magnetic-Bragg peaks are more challenging to resolve and fit. The fitted two-gaussian lineshapes were found as follows: for each temperature, we determined the positions of the (010) and $(001)'$ peaks using the fitted centers for (020) and $(002)'$,

and the full width at half maximum (FWHM) for each of the two gaussian peaks fit to $(010)/(001)'$ was determined at 200 K and kept fixed for all other temperatures.

The FWHM of each of the red and blue peaks in Fig. 8 agree with the calculated resolutions of 0.031 and 0.033 rlu (reciprocal lattice units) for (010) and (020) , respectively. The data and fits in Figs. 8(a) and 8(b) indicate that magnetic-Bragg peaks are present at both (010) and $(001)'$ below $T_{N_{Mn}}$ and that they have almost similar integrated intensities at both $T = 200$ and 50 K. The populations of the twin domains can be estimated from the differences in area of the (020) and $(002)'$ Bragg peaks in Figs. 8(e)–8(h), however, results presented below from our refinements to the TOPAZ data give a more accurate quantification of the twins' populations. This is because TOPAZ utilizes detectors that allow for simultaneous measurement of more than one dimension for each peak and because it recorded a greater number of peaks. The data for 20 and 8 K are discussed in subsequent subsections.

To summarize Fig. 6, magnetic ordering occurring at $T_{N_{Mn}}$ creates magnetic-Bragg peaks at $(hk0)$ and $(h0l)'$ positions with h even and k or l odd. Figure 7 shows the detailed temperature dependence of the height of several structural and magnetic-Bragg peaks. These data were obtained by setting the spectrometer at the center of a peak and measuring while cooling the sample through $T_{N_{Mn}}$. $80'$ collimators were utilized after the sample, and peaks with a nonzero k or l can contain intensity from the twin domain.

As stated above, the increase in intensity for the $(010)/(001)'$ and $(210)/(201)'$ peaks seen in Figs. 7(a)

TABLE I. Isotropy-magnetic subgroups and irreducible representations (Irreps) for the space group for EuMnSb_2 , $P_{n \frac{2_1}{m} \frac{2_1}{a}}^{2_1 \frac{2_1}{m} \frac{2_1}{a}}$ ($Pnma$), with Mn and Eu at Wyckoff position $4c$ and an antiferromagnetic propagation vector of $\boldsymbol{\tau} = (000)$. Yes and no indicates the presence and absence, respectively, of a magnetic-Bragg peak. The experimental observations for $T_{\text{N}_{\text{Eu}1}} < T < T_{\text{N}_{\text{Mn}}}$ and $T_{\text{N}_{\text{Eu}2}} < T < T_{\text{N}_{\text{Eu}1}}$ are given in the bottom row.

Irrep	Isotropy Magnetic Subgroups	$(h00)$ h even	$(h00)$ h odd	(010)	(001)
$m\Gamma_{1+}$	$P_{n \frac{2_1}{m} \frac{2_1}{a}}^{2_1 \frac{2_1}{m} \frac{2_1}{a}}$	no	yes	yes	yes
$m\Gamma_{2+}$	$P_{n' \frac{2_1}{m'} \frac{2_1}{a}}^{2_1' \frac{2_1}{m'} \frac{2_1}{a}}$	yes	no	no	yes
$m\Gamma_{3+}$	$P_{n \frac{2_1}{m'} \frac{2_1'}{a'}}^{2_1 \frac{2_1'}{m'} \frac{2_1'}{a'}}$	no	yes	no	no
$m\Gamma_{4+}$	$P_{n' \frac{2_1'}{m} \frac{2_1'}{a'}}^{2_1' \frac{2_1}{m} \frac{2_1'}{a'}}$	yes	no	no	no
$m\Gamma_{1-}$	$P_{n' \frac{2_1}{m'} \frac{2_1}{a}}^{2_1 \frac{2_1}{m'} \frac{2_1}{a}}$	no	yes	yes	yes
$m\Gamma_{2-}$	$P_{n \frac{2_1'}{m} \frac{2_1'}{a'}}^{2_1' \frac{2_1'}{m} \frac{2_1'}{a'}}$	yes	no	no	yes
$m\Gamma_{3-}$	$P_{n' \frac{2_1}{m'} \frac{2_1'}{a'}}^{2_1 \frac{2_1'}{m'} \frac{2_1'}{a'}}$	no	yes	no	no
$m\Gamma_{4-}$	$P_{n \frac{2_1'}{m} \frac{2_1'}{a'}}^{2_1' \frac{2_1}{m} \frac{2_1'}{a'}}$	yes	no	yes	no
	Experiment	no	yes	yes	yes

and 7(b), respectively, upon cooling below $T_{\text{N}_{\text{Mn}}} = 323(1)$ K indicates that magnetic-Bragg peaks are present at these locations. The finite intensity above $T_{\text{N}_{\text{Mn}}}$ for $(210)/(201)'$ is due to structural-Bragg peaks. Figures 7(c), 7(d), and 7(e) show that no discernible changes in intensity occur upon crossing $T_{\text{N}_{\text{Mn}}}$ for the (600) , $(020)/(002)'$, and $(220)/(202)'$ positions. We additionally did not observe the appearance of any magnetic-Bragg peaks at $(h00)$ with h odd while cooling through $T_{\text{N}_{\text{Mn}}}$. The magnetic-Bragg peaks can be analyzed using an AFM propagation vector of $\boldsymbol{\tau} = (0,0,0)$. This AFM propagation vector means that the magnetic-unit and chemical-unit cells have the same dimensions.

Consistent with Landau theory, a second-order (continuous) phase transition will decrease the symmetry of a system accordant with a group-subgroup relation. We used ISODISTORT [28, 29] to determine the irreducible representations for magnetic order consistent with space group $P_{n \frac{2_1}{m} \frac{2_1}{a}}^{2_1 \frac{2_1}{m} \frac{2_1}{a}}$ and $\boldsymbol{\tau} = (0,0,0)$ with magnetic Eu and Mn at the $4c$ Wyckoff position. Table I shows the results, where each irreducible representation corresponds to an isotropy-magnetic subgroup of $P_{n \frac{2_1}{m} \frac{2_1}{a}}^{2_1 \frac{2_1}{m} \frac{2_1}{a}}$. We find that out of the eight irreducible representations both $m\Gamma_{1+}$ and $m\Gamma_{1-}$ allow for the existence of magnetic-Bragg peaks at both (010) and $(001)'$ as seen in Figs. 8(a) and 8(b). $m\Gamma_{1+}$ is ruled out because it only allows for $\boldsymbol{\mu} \parallel \mathbf{b}$ which would necessitate magnetic-Bragg peaks at $(h00)$, h odd, positions. This leaves $m\Gamma_{1-}$ and magnetic space group (MSG) $P_{n' \frac{2_1}{m'} \frac{2_1}{a}}^{2_1' \frac{2_1}{m'} \frac{2_1}{a}}$.

Determination of whether the Mn, Eu, or both order below $T_{\text{N}_{\text{Mn}}}$ requires comparing the integrated intensities of the magnetic-Bragg peaks to those calculated for trial magnetic structures. Fortunately, the $4c$ Wyckoff positions occupied by Mn and Eu make the intensity of certain magnetic-Bragg peaks very sensitive to the direction of $\boldsymbol{\mu}$ and the positions of the magnetic atoms. We first discuss some general obser-

vations we can make about the possible AFM structure and then present results from a single-crystal refinement that determined the AFM structure.

MSG $P_{n' \frac{2_1}{m'} \frac{2_1}{a}}^{2_1' \frac{2_1}{m'} \frac{2_1}{a}}$ allows for $\boldsymbol{\mu}$ to have components lying within the ac plane. The existence of the (010) and $(001)'$ magnetic-Bragg peaks points to $\boldsymbol{\mu}$ having a component along \mathbf{a} whereas the absence of magnetic-Bragg peaks for $(h00)$, h odd, means that the component of $\boldsymbol{\mu}$ along \mathbf{c} is zero. To consider whether both or either $\boldsymbol{\mu}_{\text{Mn}}$ and $\boldsymbol{\mu}_{\text{Eu}}$ have a finite component along \mathbf{a} , we simulated diffraction patterns using trial structures consistent with $P_{n' \frac{2_1}{m'} \frac{2_1}{a}}^{2_1' \frac{2_1}{m'} \frac{2_1}{a}}$. We found that magnetic-Bragg peaks existing at both (210) and $(201)'$ with no magnetic-Bragg peaks at (220) and $(202)'$ would indicate a component of $\boldsymbol{\mu}_{\text{Mn}}$ lying along \mathbf{a} . On the other hand, no magnetic-Bragg peak at $(210)/(201)'$ but a magnetic Bragg peak at $(220)/(202)'$ would indicate a component of $\boldsymbol{\mu}_{\text{Eu}}$ lying along \mathbf{a} . From Figs. 6(e) and 6(g) we see that a magnetic-Bragg peak occurs only at $(210)/(201)'$. Next, if both the Mn and Eu moments were ordered along \mathbf{a} we find that (010) and $(001)'$ would have very dissimilar intensities. Figures 8(a) and 8(b) show that this is not the case. This means that, within our limit of detection, only AFM ordering of the Mn occurs upon cooling through $T_{\text{N}_{\text{Mn}}}$ with $\boldsymbol{\mu}_{\text{Mn}}$ lying along \mathbf{a} .

The magnetic structure was fully determined by single-crystal refinements using 1944 structural and 70 magnetic-Bragg peaks recorded on TOPAZ at $T = 50$ K. The best refinement yielded MSG $P_{n' \frac{2_1}{m'} \frac{2_1}{a}}^{2_1' \frac{2_1}{m'} \frac{2_1}{a}}$ with $\mu_{\text{Mn}} = 3.0(2) \mu_{\text{B}}$ lying along \mathbf{a} and $\text{GOF} = 6.80$. The AFM order is C-type, as shown in Fig. 1(e). The goodness-of-fit parameter is defined as $\text{GOF} = [\sum w(F_o - F_c)^2 / (m - n)]^{1/2}$ where the sum is over the recorded integrated intensities of the Bragg peaks, F_o is the observed value of the structure factor determined from the integrated intensities, F_c is the calculated value of the structure factor, m is the total number of Bragg peaks used, n is the number of refined parameters, and w is the reciprocal of the sum of a spectrometer specific parameter and the variance associated with each value of F_o . A plot of F_c versus F_o is shown in Fig. 9(a) and Figs. 9(b) and 9(c) show simulated diffraction patterns for the AFM structure. Other than the exact value for μ_{Mn} , the AFM structure we find for $T_{\text{N}_{\text{Eu}1}} < T < T_{\text{N}_{\text{Mn}}}$ is the same as those previously reported for both powder and single-crystal samples [15–17].

The TOPAZ data cover far more of \mathbf{Q} space than our triple-axis measurements and therefore present far more Bragg peaks. Consistent with the triple-axis data in Fig. 8, the TOPAZ data also indicate that presence of two twins where the b and c axes are switched between the twins. Our refinement to the TOPAZ data finds that the populations of the two twin domains are 60% and 40% with an uncertainty of 1%.

2. $T_{\text{N}_{\text{Eu}1}} > T > T_{\text{N}_{\text{Eu}2}}$

Figures 10 and 11 show that additional magnetic-Bragg peaks emerge below $T_{\text{N}_{\text{Eu}1}}$ and $T_{\text{N}_{\text{Eu}2}}$. They are due to AFM ordering transitions at $T_{\text{N}_{\text{Eu}1}} = 23(1)$ K and $T_{\text{N}_{\text{Eu}2}} = 9(1)$ K. We describe our determination of the magnetic order below

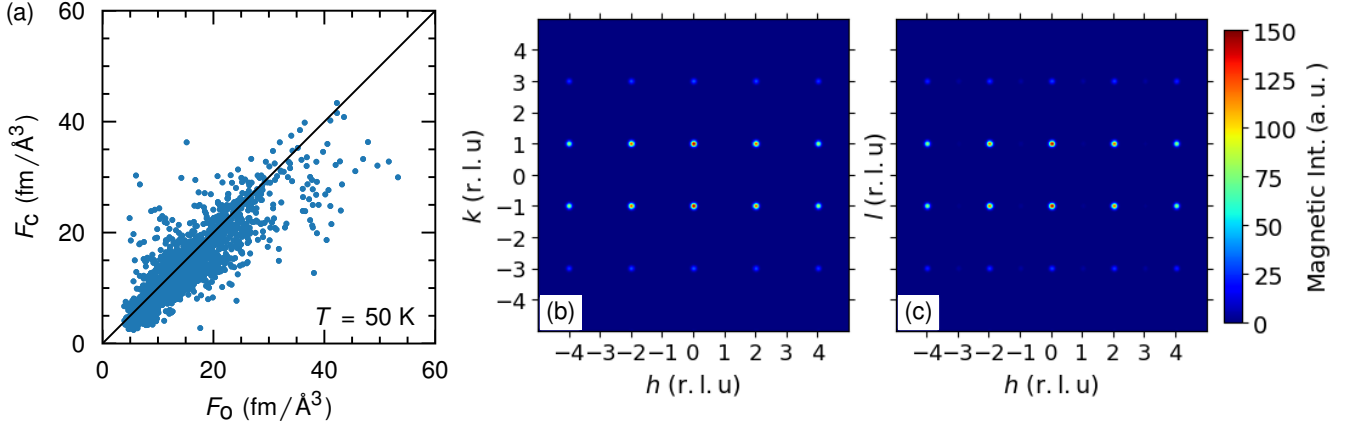


FIG. 9. (a) The calculated versus observed structure factors for both nuclear and magnetic Bragg peaks from a refinement to $T = 50 \text{ K}$ data for EuMnSb_2 taken on TOPAZ using the antiferromagnetic structure in Fig. 1(e). [(b), (c)] Simulated $(hk0)$ (b) and $(h0l)$ (c) diffraction patterns for the 50 K antiferromagnetic order made with MAG2POL [22].

T_{NEu1} in this subsection and our determination of the magnetic order below T_{NEu2} in the next subsection.

New magnetic-Bragg peaks appear at $(h00)$, h odd, positions when cooling below T_{NEu1} , as seen for (300) in Fig. 10(a) and 11(a). Magnetic-Bragg peaks are allowed at these positions for MSG $P_{n'}^{2_1} \frac{2_1}{m'} \frac{2_1}{a'}$. Similar to the higher temperature data, the lines in Fig. 10 show fits to either a gaussian [Figs. 10(a)–10(c), 10(g), and 10(h)] or two-gaussian lineshape [Figs. 10(d)–10(f)].

Data in Fig. 10(b) show that the $(010)/(001)'$ magnetic-Bragg peak continues to grow upon cooling below T_{NEu1} . Data in Fig. 8(c) reveal that it is the (010) magnetic-Bragg peak that continues to grow upon cooling below T_{NEu1} whereas the $(001)'$ peak decreases. Thus, the change in slope of the data in Fig. 11(b) is due to an increase in the height of the (010) magnetic-Bragg peak with decreasing T below T_{NEu1} . There is no sharp change in intensity associated with crossing T_{NEu1} for either (600) or $(020)/(002)'$ as shown in Figs. 10(c) and 11(c) for (600) and Figs. 8(f), 8(g), 10(d) and 11(d) for $(020)/(002)'$. All of these observations are consistent with the reflection conditions for MSG $P_{n'}^{2_1} \frac{2_1}{m'} \frac{2_1}{a'}$.

Next, Figs. 10(e) and 11(e) indicate that a magnetic-Bragg peak appears at $(120)/(102)'$ below T_{NEu1} . Weak peaks are also present at 30 K which indicates that shorter-range magnetic correlations exist at $T > T_{\text{NEu1}}$. As we describe below, the presence of such short-range correlations is consistent with the Mössbauer and C_p data. The existence of a magnetic-Bragg peak at (120) or $(102)'$ is also consistent with MSG $P_{n'}^{2_1} \frac{2_1}{m'} \frac{2_1}{a'}$, as is a magnetic-Bragg peak at (220) or $(202)'$. Data for $(220)/(202)'$ are shown in Figs. 10(f) and 11(f).

Finally, Figs. 10(g) and 11(g) show that a magnetic-Bragg peak(s) emerges at $(110)/(101)'$ upon cooling below T_{NEu1} whereas data in Figs. 10(h) and 11(h) show no increase in the magnetic-Bragg peak at $(210)/(201)'$. Magnetic-Bragg peaks at (110) and $(101)'$ are allowed for MSG $P_{n'}^{2_1} \frac{2_1}{m'} \frac{2_1}{a'}$. Similar to our above discussion for $(120)/(102)'$, the weak peak apparent at $(101)'$ in Fig. 10(g) for 30 K indicates that magnetic correlations begin forming above T_{NEu1} .

Having established that the magnetic-Bragg peaks existing for $T_{\text{NEu2}} < T < T_{\text{NEu1}}$ are consistent with the reflection conditions for MSG $P_{n'}^{2_1} \frac{2_1}{m'} \frac{2_1}{a'}$, we next discuss some general considerations for the AFM structure and then present results from single-crystal refinements. First, for this MSG magnetic-Bragg peaks existing at $(h00)$, h odd, means that either or both μ_{Mn} and μ_{Eu} have a component along c . From simulated diffraction patterns, we find that the increase in integrated intensities for the (110) and $(101)'$ magnetic-Bragg peaks is only sensitive to an increase in μ_{Eu} lying along c . Thus, the increase in height of the $(110)/(101)'$ magnetic-Bragg peak when cooling below T_{NEu1} which is evident in Figs. 10(g) and 11(g) is due to the development of a finite component of μ_{Eu} along c . This does not, however, strictly rule out that μ_{Mn} also develops a component along c .

Next, data in Fig. 8(c) show that the height of the (010) magnetic-Bragg peak greatly increases upon cooling through T_{NEu1} whereas the height of the $(001)'$ magnetic-Bragg peak decreases. The simplest explanation for these observations is that μ_{Eu} develops a finite component parallel to a as well as a component along c . These observations do not rule out, however, that the component of μ_{Mn} along a also increases below T_{NEu1} .

Since both μ_{Mn} and μ_{Eu} have finite components along a , the effects due to interference between the Eu and Mn magnetic sublattices on the magnetic structure factor must be taken into account. Thus, one must consider the cases of nearest-neighboring μ_{Mn} and μ_{Eu} having a components aligned either parallel or antiparallel to one another. This is referred to as the phase between the two magnetic sublattices. Our calculations for the (010) and $(001)'$ magnetic-Bragg peak heights demonstrate sensitivity to this phase. Based on these simulations and the data in Fig. 8(c) indicating that the height of the (010) magnetic-Bragg peak increases below T_{NEu1} whereas the height of the $(001)'$ magnetic-Bragg peak decreases, we determined that the a components of μ_{Mn} and μ_{Eu} point antiparallel to each other.

We performed single-crystal refinements to our $T = 12 \text{ K}$

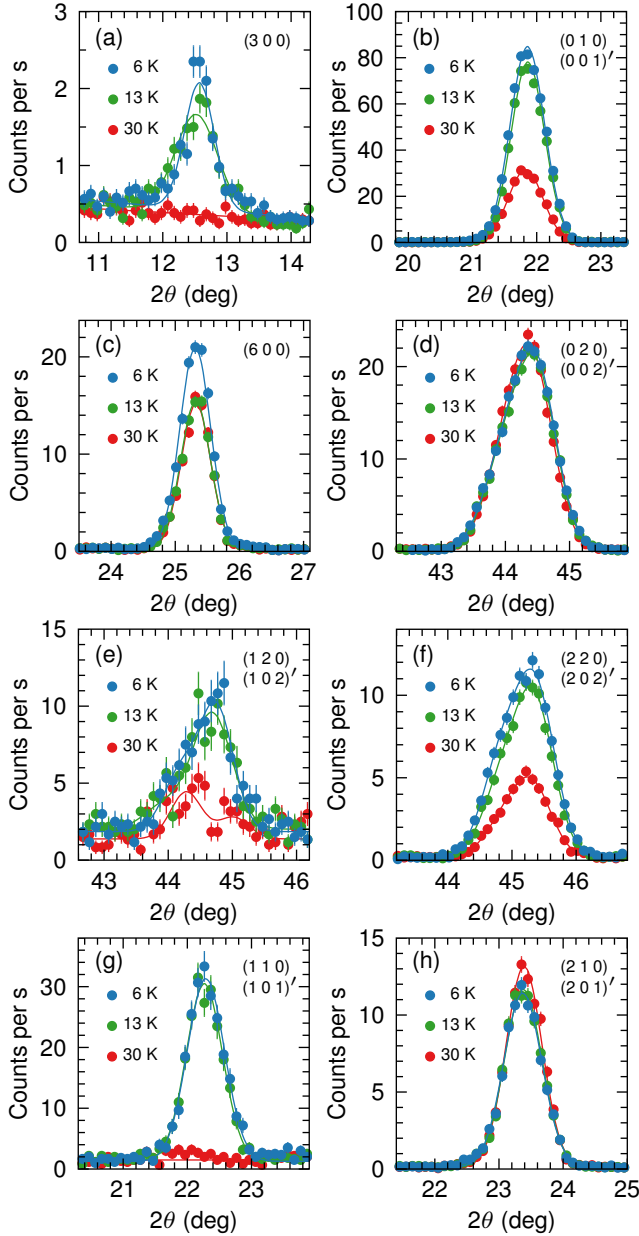


FIG. 10. Data for EuMnSb_2 from longitudinal (θ - 2θ) scans across the (300) (a), (010)/(001)' (b), (600)/(600)' (c), (020)/(002)' (d), (120)/(102)' (e), (220)/(202)' (f), (110)/(101)' (g), and (210)/(201)' (h) positions at $T = 30$, 13, and 6 K. Lines are fits to either the gaussian or two gaussian lineshapes with constant offsets described in the text.

TOPAZ data using 5330 nuclear and 374 magnetic Bragg peaks and various test magnetic structures. The best refinement gave MSG $P_{n' m' a'}^{2_1 2_1 2_1}$ and kept the higher temperature Mn sublattice order. The GOF is 6.11. The refinement found $\mu_{\text{Eu}} = 4.7(2) \mu_{\text{B}}$ with $\mu_{\text{Eu}} = 4.0(2) \mu_{\text{B}}$ along \mathbf{a} and $\mu_{\text{Eu}} = 2.4(2) \mu_{\text{B}}$ along \mathbf{c} . This gives a canting angle of $\phi_{\text{ac}} = 31(1)^\circ$ away from \mathbf{a} at 12 K towards \mathbf{c} , which is somewhat less than the value of $\phi_{\text{ac}} = 41(1)^\circ$ found in Ref. [16] for 7 K. A plot of F_c versus F_o is shown in Fig. 12(a) and Figs. 12(b) and

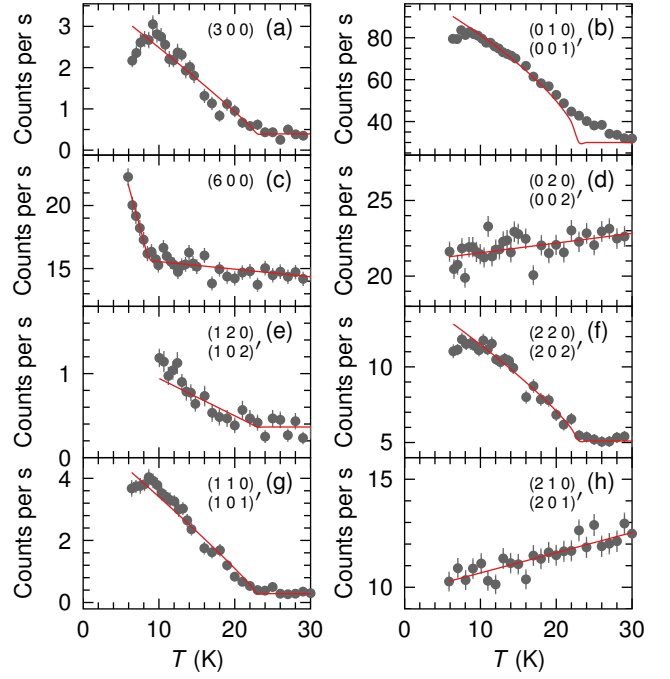


FIG. 11. The intensities of the (300) (a), (010)/(001)' (b), (600) (c), (020)/(002)' (d), (120)/(102)' (e), (220)/(202)' (f), (110)/(101)' (g), and (210)/(201)' (h) Bragg peaks for EuMnSb_2 as functions of temperature. A sharp change in intensity below T_{NEu1} and/or T_{NEu2} is due to magnetic ordering. Lines are guides to the eye.

12(c) show simulated diffraction patterns corresponding to the AFM structure. The AFM structure is illustrated in Fig. 1(f). For completeness, a refinement made using the opposite phase between the Mn and Eu magnetic sublattices resulted in a slightly worse GOF of 6.14 with $\mu_{\text{Eu}} = 3.6(2) \mu_{\text{B}}$ along \mathbf{a} and $\mu_{\text{Eu}} = 2.4(2) \mu_{\text{B}}$ along \mathbf{c} .

3. $T < T_{\text{NEu2}}$

Additional magnetic-Bragg peaks emerge upon cooling below $T_{\text{NEu2}} = 9(1) \text{ K}$ at $(h00)$, h even, positions. This is shown in Figs. 10(c) and 11(c) for (600). Accompanying the appearance of these new magnetic-Bragg peaks is a decrease in the height of the (300) magnetic-Bragg peak, as shown in Fig. 11(a). Figures 11(b), 11(f), and 11(g) show that the (010)/(001)', (220)/(202)', and (110)/(101)' magnetic-Bragg peaks either slightly decrease or remain constant upon cooling below T_{NEu2} . Data in Figs. 11(d) and 11(h) indicate that heights of the (020)/(002)' and (210)/(201)' peaks show no response to cooling through T_{NEu2} .

The appearance of magnetic-Bragg peaks at $(h00)$, h even, is inconsistent with MSG $P_{n' m' a'}^{2_1 2_1 2_1}$. In addition, Table I shows that no MSGs that are maximal-isotropy subgroups of space group $P_{n m a}^{2_1 2_1 2_1}$ with $\tau = (0, 0, 0)$ and Mn and Eu at the $4c$ Wyckoff position allow for the simultaneous appearance of $(h00)$, h even, and $(h00)$, h odd, magnetic-Bragg

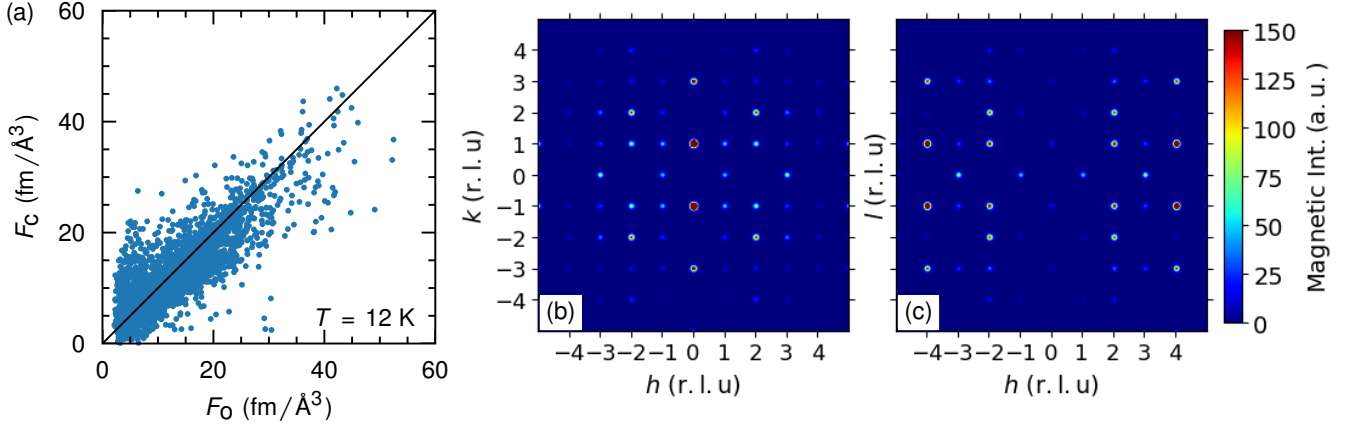


FIG. 12. (a) The calculated versus observed structure factors for both nuclear and magnetic Bragg peaks from a refinement to $T = 12$ K data for EuMnSb_2 taken on TOPAZ using the antiferromagnetic structure in Fig. 1(f). [(b), (c)] Simulated $(hk0)$ (b) and $(h0l)$ (c) diffraction patterns for the 12 K antiferromagnetic order made with MAG2POL [22].

TABLE II. Maximal-isotropy-magnetic subgroups of magnetic space group $P\frac{2_1}{n'}\frac{2_1}{m'}\frac{2_1}{a'}$ for EuMnSb_2 with $\tau = (000)$ and Mn and Eu at the $4c$ Wyckoff position. The subgroups are given in the setting of $P\frac{2_1}{n}\frac{2_1}{m}\frac{2_1}{a}$.

Isotropy Magnetic Subgroups of $P\frac{2_1}{n'}\frac{2_1}{m'}\frac{2_1}{a'}$
$P2_1\frac{2_1}{m'}\frac{2_1}{a'}$
$P2_12_12_1$
$P\frac{2_1}{n'}11$
$P1\frac{2_1}{m'}1$
$P\frac{2_1}{n'}\frac{2_1}{m'}2_1$
$P\frac{2_1}{n'}2_1\frac{2_1}{a'}$
$P11\frac{2_1}{a'}$

peaks. Therefore, it is necessary to consider lower-symmetry MSGs. To this end, Table II shows the maximal-isotropy subgroups for MSG $P\frac{2_1}{n'}\frac{2_1}{m'}\frac{2_1}{a'}$ with $\tau = (0, 0, 0)$ and Mn and Eu at the $4c$ Wyckoff position.

We can immediately exclude MSGs $P2_1\frac{2_1}{m'}\frac{2_1}{a'}$, $P2_12_12_1$, and $P\frac{2_1}{n'}11$ since they forbid magnetic-Bragg peaks at $(h00)$, h even. We then tested our data against calculations for various trial magnetic-moment configurations under MSG $P1\frac{2_1}{m'}1$, which corresponds to the MSG found in Ref. [15] for the low-temperature AFM structure but in a different crystallographic setting. We found that μ_{Mn} would need to develop a significant FM component along c to produce a magnetic-Bragg peak at (300) with the height observed in Fig. 10(a). This would also require much weaker magnetic-Bragg peaks at $(110)/(101)'$ than we observe in Fig. 10(g): the intensity of (110) would be zero and the intensity of $(101)'$ would be quite weak. Thus, we found it unlikely that MSG $P1\frac{2_1}{m'}1$ describes the AFM order below $T_{\text{NEu}2}$ for our sample.

We next made single-crystal refinements using the MSGs in Table II and trial ordered-moment configurations in order

to determine the AFM structure at $T = 5$ K. The refinements used 4573 nuclear and 321 magnetic-Bragg peaks recorded on TOPAZ. The results indicated that MSG $P11\frac{2_1}{a'}$ with lattice angles $\alpha = \beta = \gamma = 90^\circ$ best describes the AFM structure with the higher temperature AFM order of the Mn magnetic sublattice maintained. The ratios of the four domains present for the MSG were set to 30%:30%:20%:20% which is in line with the twin populations found at 50 K.

The best refinement found that μ_{Eu} develops a component along b below $T_{\text{NEu}2}$. The components of μ_{Eu} are found to be $2.4(4)$, $4.3(2)$, and $2.6(2)$ μ_{B} lying along a , b , and c , respectively. This gives a total Eu-ordered-magnetic moment of $\mu_{\text{Eu}} = 5.6(4)$ μ_{B} . The GOF parameter is 6.19, which is similar to the value found for the higher temperature AFM phases. The magnetic structure is shown in Fig. 1(g) and Fig. 13(a) shows the results of the refinement. Figures 13(b) and 13(c) show simulated diffraction patterns corresponding to the AFM structure.

To test other possible solutions, a refinement made with the components of μ_{Eu} along a and c fixed to those found at $T = 12$ K [$4.0(2)$ μ_{B} and $2.4(2)$ μ_{B} along a and c , respectively] results in a worse GOF of 6.22 and a component of μ_{Eu} along b of $3.5(2)$ μ_{B} . The magnitude of μ_{Eu} found from both refinements is similar, being $\mu_{\text{Eu}} = 5.6(4)$ μ_{B} for the former and $5.8(2)$ μ_{B} for the latter.

As for the other two MSGs not yet ruled out, a refinement using MSG $P\frac{2_1}{n'}\frac{2_1}{m'}2_1$ yields a similar GOF but does not give a value of the R factor for the magnetic part of the refinement that is lower than that we obtain for our best refinement for MSG $P11\frac{2_1}{a'}$. R is defined as $R = \sum_i |y_i(\text{obs}) - y_i(\text{calc})| / y_i(\text{obs})$ where $y_i(\text{obs})$ and $y_i(\text{calc})$ correspond to the observed and calculated integrated intensities for the measured peak i . For MSG $P\frac{2_1}{n'}2_1\frac{2_1}{a'}$, the best refinement gives similar values for R and GOF as our best refinement using MSG $P11\frac{2_1}{a'}$, but it indicates a net \mathbf{M} along b with a component of μ_{Eu} along b of $1.5(3)$ μ_{B} . However, the absence of a clear increase in the intensity of the $(002)'$ peak in Figs. 8(h), 10(d), and 11(d) upon cooling below $T_{\text{NEu}2}$ tends to rule out

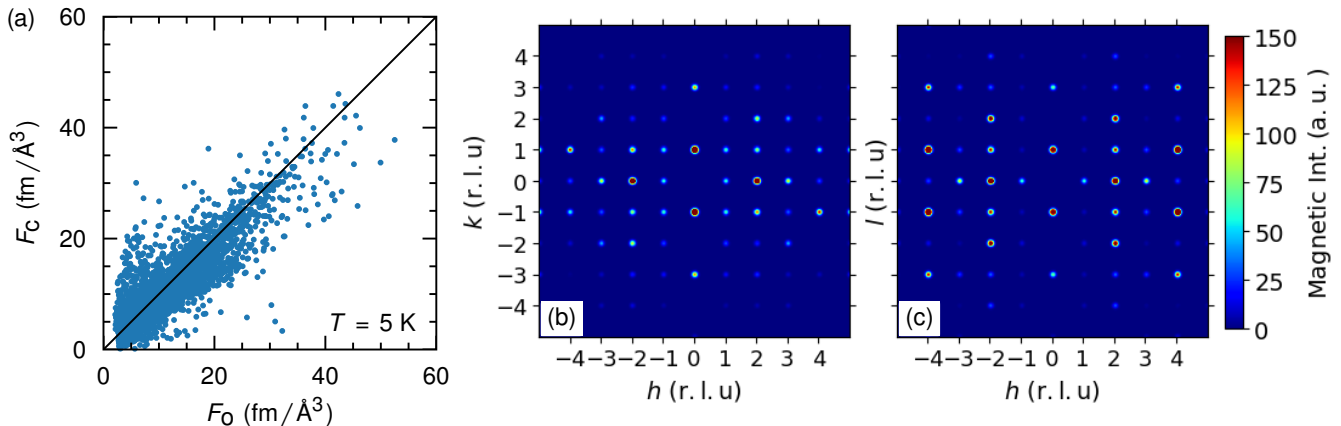


FIG. 13. (a) The calculated versus observed structure factors for both nuclear and magnetic Bragg peaks from a refinement to $T = 5$ K data for EuMnSb_2 taken on TOPAZ using the antiferromagnetic structure in Fig. 1(g). [(b), (c)] Simulated $(hk0)$ (b) and $(h0l)$ (c) diffraction patterns for the 5 K antiferromagnetic order made with MAG2POL [22].

this MSG.

Table III summarizes the parameters in each AFM phase determined from our best refinements. Lattice parameters for various temperatures are also included. The value of $\mu_{\text{Eu}} = 5.6(4) \mu_{\text{B}}$ we find for $T = 5$ K is lower than the full value of $7 \mu_{\text{B}}$ expected for Eu^{2+} . μ_{Eu} may further increase upon cooling below 5 K, however, an increase of $1.2 \mu_{\text{B}}$ between 5 and 0 K is not expected by the curves in Fig. 11. On the other hand, $M(\mu_0 H)$ data for EuMnBi_2 taken up to $\mu_0 H = 52$ T find a saturated moment at $\mu_0 H = 22$ T and $T = 1.4$ K of only $6.4 \mu_{\text{B}}$ [14]. This suggests $\mu_{\text{Eu}} < 7 \mu_{\text{B}}$ for this structurally related compound. Similar high-field measurements to determine the saturated moment for EuMnSb_2 should be insightful.

We must also consider that the significant neutron absorption due to ^{151}Eu negatively affects the accuracy and precision with which we can determine μ_{Eu} and μ_{Mn} as well as other parameters. Lower than expected values for μ_{Eu} as determined by neutron diffraction have been reported for other Eu-containing compounds [30], including previous studies on EuMnSb_2 which found that $\mu_{\text{Eu}} = 5.9(8) \mu_{\text{B}}$ at 7 K [16] and $\mu_{\text{Eu}} = 5.2(4) \mu_{\text{B}}$ at 5 K [17]. For our measurements, we used standard algorithms to mitigate and correct for the absorption effects. However, while good, these algorithms are imperfect and make determining the exact uncertainty associated with certain parameters, such as μ_{Eu} and μ_{Mn} , problematic. The uncertainty values for U_{iso} , x , y , z , μ_{Mn} , μ_{Eu} , and the components of $\boldsymbol{\mu}_{\text{Eu}}$ quoted in Table III correspond to one standard deviation from their refined values. The actual uncertainty is likely larger and difficult to precisely quantify.

Finally, regarding the Mössbauer data presented in Section III C and the presence of short-range magnetic correlations, such correlations would give rise to weak and broad magnetic diffraction peaks. These peaks would be difficult to resolve below $T_{\text{N}_{\text{Eu}1}}$ in the midst of AFM Bragg peaks via typical neutron diffraction measurements. The presence of thermal-neutron absorbing Eu in EuMnSb_2 would further diminish the ability to detect such weak peaks. Nevertheless, as

noted above, there is some evidence in our diffraction data [e.g. the shape of the order-parameter curve upon crossing $T_{\text{N}_{\text{Eu}1}}$ in Fig. 11(b)] for short-range magnetic correlations existing above $T_{\text{N}_{\text{Eu}1}}$. The $C_p(T)$ data in Fig. 3 exhibit a broad peak at $T_{\text{N}_{\text{Eu}1}}$ which is also consistent with the presence of short-range magnetic correlations, although subtle structural disorder not resolved in our neutron diffraction, x-ray diffraction, and EDS measurements could also broaden the peak.

IV. DISCUSSION

Based on our results, we can make some general conclusions about the microscopic magnetic interactions in the compound. We start by using the determined AFM structures to make some assumptions about a minimal Heisenberg model for the compound that includes single-ion magnetic anisotropy. This model has the generic form

$$\mathcal{H} = \sum_{i,j} \tilde{S}_i J_{ij} S_j + \sum_i \tilde{S}_i D_i S_i, \quad (2)$$

where J is the magnetic exchange, D is magnetic anisotropy, i and j label magnetic ions, and S is spin. The AFM order of the Mn planes above $T_{\text{N}_{\text{Eu}1}}$ suggests AFM intralayer exchange for NN Mn spins within a plane, FM interlayer exchange between NN Mn layers, and Mn easy-axis anisotropy preferring the a direction. These considerations hold for all temperatures.

The AFM order of the Eu sublattice below both $T_{\text{N}_{\text{Eu}1}}$ and $T_{\text{N}_{\text{Eu}2}}$ points to dominant FM NN intralayer exchange. The NN interlayer exchange between Eu layers depends on whether a Sb1-Mn-Sb1 block or a Sb2 layer separates the Eu layers. For both cases, the a and b components of the Eu interlayer exchange are AFM. However, the c component of the Eu interlayer exchange is FM across Sb1-Mn-Sb1 blocks and AFM across Sb2 layers. The appearance of a finite component of $\boldsymbol{\mu}_{\text{Eu}}$ along b below $T_{\text{N}_{\text{Eu}2}}$ rather than $T_{\text{N}_{\text{Eu}1}}$ suggests that the b

TABLE III. Structural and magnetic parameters for orthorhombic EuMnSb_2 at various temperatures. All of the atoms occupy the $4c$ Wyckoff position of space group $Pnma$ ($P_{\frac{2_1}{n} \frac{2_1}{m} \frac{2_1}{a}}$). The parameters are from refinements made to data taken on TOPAZ. $\mu_{\text{Eu-a}}$, $\mu_{\text{Eu-b}}$, and $\mu_{\text{Eu-c}}$ are the components of the ordered Eu magnetic moment μ_{Eu} along \mathbf{a} , \mathbf{b} , and \mathbf{c} , respectively. GOF is the goodness-of-fit parameter for the combined nuclear and magnetic refinements and is defined in the text. MSG stands for magnetic space group. The best refinements found that the ordered Mn magnetic moment μ_{Mn} lies along \mathbf{a} and that the antiferromagnetic order of the Mn sublattice found at 50 K remains unchanged for 12 and 5 K. The structural parameters U_{iso} , x , y , and z determined at 50 K were also used for 12 and 5 K, as well as the refined values for the twin populations of 60(1)% and 40(1)%. x , y , and z are given in the basis of space group $P_{\frac{2_1}{n} \frac{2_1}{m} \frac{2_1}{a}}$.

	$T = 50$ K	12 K	5 K
a (Å)	22.4958(1)	22.4928(2)	22.4927(2)
b (Å)	4.3758(1)	4.3787(1)	4.3773(1)
c (Å)	4.3908(1)	4.3791(1)	4.3802(1)
V (Å ³)	431.45(1)	431.29(1)	431.26(1)
Eu U_{iso}	0.0066(3)	0.0066	0.0066
Eu x	0.38598(6)	0.38598	0.38598
Eu y	0.25	0.25	0.25
Eu z	0.7712(9)	0.7712	0.7712
Mn U_{iso}	0.0070(4)	0.0070	0.0070
Mn x	0.2501(3)	0.2501	0.2501
Mn y	0.25	0.25	0.25
Mn z	0.271(2)	0.271	0.271
Sb 1 U_{iso}	0.0044(3)	0.0044	0.0044
Sb 1 x	0.32545(6)	0.32545	0.32545
Sb 1 y	0.75	0.75	0.75
Sb 1 z	0.2727(9)	0.2727	0.2727
Sb 2 U_{iso}	0.0044(3)	0.0044	0.0044
Sb 2 x	0.4984(1)	0.4984	0.4984
Sb 2 y	0.25	0.25	0.25
Sb 2 z	0.2813(9)	0.2813	0.2813
μ_{Mn} (μ_{B})	3.0(2)	3.0	3.0
μ_{Eu} (μ_{B})	0	4.7(2)	5.6(4)
$\mu_{\text{Eu-a}}$ (μ_{B})	0	4.0(2)	2.4(4)
$\mu_{\text{Eu-b}}$ (μ_{B})	0	0	4.3(2)
$\mu_{\text{Eu-c}}$ (μ_{B})	0	2.4(1)	2.6(1)
GOF	6.80	6.11	6.19
MSG	$P_{\frac{2_1}{n'} \frac{2_1}{m'} \frac{2_1}{a'}}$	$P_{\frac{2_1}{n'} \frac{2_1}{m'} \frac{2_1}{a'}}$	$P11_{\frac{2_1}{a'}}$

component of the interlayer Eu exchange is smaller than the other exchange terms. It is also possible that the Eu anisotropy changes with decreasing temperature such that the tendency for μ_{Eu} to lie mostly along \mathbf{a} weakens with decreasing T , especially upon crossing below T_{NEu2} .

The NN interlayer exchange between Eu and Mn may be weak, since based on the diffraction results the Eu ordering does not appear to affect the Mn sublattice order. However, as discussed below, this would differ with a reported result for the related compound EuMnBi_2 which finds substantial Eu-Mn coupling based on $M(H)$ data [31]. Inelastic neutron scattering measurements to determine the magnetic interactions from fits to the spin-wave spectrum are a typical way to sort out the magnetic Hamiltonian. However, the thermal-neutron absorbing properties of ¹⁵¹Eu and its $\approx 48\%$ natural abundance will make planning and performing such measure-

ments especially challenging.

Considering the different AFM structures found below T_{NEu1} by powder neutron diffraction [15] and the report of only two AFM phases down to $T = 7$ K from previous single-crystal neutron diffraction data [16], the finding of a third AFM phase in our samples begs questions concerning the sensitivity of the magnetism to stoichiometry or other aspects of the chemical structure. Indeed, Ref. 17 presents a study of single crystals for the series $\text{Eu}_{1-x}\text{Sr}_x\text{MnSb}_2$ and finds a tetragonal chemical unit cell [space group $P_{\frac{4}{n}}^2mm$ with $a = 4.343(6)$ Å and $c = 11.17(1)$ Å at 5 K] for $x = 0$. A 5% Mn deficiency is reported for the tetragonal parent compound ($\text{EuMn}_{0.95}\text{Sb}_2$), and the orthorhombic chemical unit cell is found for $x = 0.2$ [17]. The results suggest sensitivity of both the chemical-unit cell and the AFM order to stoichiometry.

The structures of the AFM order above T_{NEu2} for our sample are consistent with those previously found for other single-crystal orthorhombic EuMnSb_2 samples [16]. Other than the phase between the magnetic sublattices, our $T > T_{\text{NEu2}}$ AFM structures are also consistent with those for orthorhombic $\text{Eu}_{0.8}\text{Sr}_{0.2}\text{MnSb}_2$ [17]. A third AFM transition is also seen in $\text{Eu}_{0.8}\text{Sr}_{0.2}\text{MnSb}_2$ below 7 K. However, it is associated with a change in the ordering of the \mathbf{c} component of μ_{Eu} from $\rightarrow\rightarrow\leftarrow\leftarrow$ to $\rightarrow\leftarrow\rightarrow\leftarrow$, which is different than the AFM order we find in our EuMnSb_2 sample below T_{NEu2} . Notably, with increasing x for $\text{Eu}_{1-x}\text{Sr}_x\text{MnSb}_2$, μ_{Eu} rotates towards \mathbf{a} with $\phi_{\text{ac}} = 0^\circ$ for $x = 0.8$, and a third (lower temperature) phase transition is not observed for $x = 0.5$ and 0.8 [17]. A component of μ_{Eu} lying along \mathbf{b} is not reported for the series. To the best of our knowledge, our findings are the first report of a finite component of μ_{Eu} along \mathbf{b} in EuMnSb_2 . To explore the tunability of the magnetism, future work should determine what parameters create the existence of a \mathbf{b} component for μ_{Eu} .

Next, we once again consider EuMnBi_2 , which has a tetragonal unit cell with space group $I_{\frac{4}{m}}^2mm$ [31] and hosts Dirac fermions within its $X2$ ($X = \text{Bi}$) layers [14]. This compound exhibits AFM ordering of the Mn and Eu moments below ≈ 315 and 22 K, respectively, with both μ_{Mn} and μ_{Eu} lying along \mathbf{c} [31]. The Mn sublattice consists of AFM alignment of NN Mn within each Mn layer but AFM alignment between Mn layers instead of the FM interlayer alignment we observe in EuMnSb_2 . The AFM structure of the Eu sublattice has an $\uparrow\uparrow\downarrow\downarrow$ stacking of FM Eu layers along \mathbf{c} [32] which also differs from the $\downarrow\uparrow\downarrow\uparrow$ configuration of the \mathbf{a} component of μ_{Eu} we observe for EuMnSb_2 . The AFM structures are similar, however, in that the Eu layers sandwiching the $X2$ layers are AFM aligned. The dominant AFM intralayer Mn exchange and FM intralayer Eu exchange suggests that an orthorhombic distortion of the tetragonal lattice does not change the sign of the intralayer Mn and Eu exchange since the same is found for EuMnSb_2 .

Below $T = 22$ K a spin-flop transition is seen in $M(H)$ for EuMnBi_2 at $\mu_0 H \approx 5.4$ T for $\mathbf{H} \parallel \mathbf{c}$ which reorients μ_{Eu} into the \mathbf{ab} plane [31, 33]. μ_{Eu} becomes fully polarized along \mathbf{H} above ≈ 22 T at ≈ 2 K where M is taken to be close to the expected fully saturated value of $7 \mu_{\text{B}}$ even though it

only reaches $6.4 \mu_B$ [14]. The absence of a clear signature for a spin-flop transition at 1.8 K in our data for EuMnSb_2 [Fig. 2(b)] can be explained by μ_{Eu} already having canted away from **a**.

The interlayer-longitudinal resistivity ρ_{zz} for EuMnBi_2 is seen to greatly depend on the magnetic order of the Eu sublattice, as ρ_{zz} is almost independent of field above 22 K, and below 22 K a large enhancement in ρ_{zz} within the spin-flop region of the phase diagram is seen along with the half-integer-quantum-Hall effect [14, 32]. The exact microscopic mechanism behind the enhancement is not clear, however, as well as the exact role of the Mn magnetic sublattice [14, 33]. The transverse magnetoresistance ρ_{xx} is found to be large and positive [14]. It is linear in H at 50 K, and quantum oscillations are superimposed on the linear magnetoresistance with a large enhancement of the height of the oscillations occurring at magnetic fields in the spin-flop region for 1.4 K [14].

For EuMnSb_2 , interlayer-longitudinal-resistivity data reported in Refs. [15] and [16] for single-crystal samples indicate a loss of spin-disorder scattering upon cooling below $T_{\text{N}_{\text{Eu1}}}$ at $\mu_0 H = 0$ T. Reference [15] also reports an $\approx 300\%$ increase in resistance with increasing field with a maximum at ≈ 5 T at $T = 2$ K, with negative magnetoresistance occurring for higher values of $\mu_0 H$. Angular dependent measurements made at 2 K show that as the field is increased the interlayer-longitudinal resistivity exhibits growing anisotropy, with clear peaks when the angle between **a** and **b** is $\phi_{\text{ab}} = 0^\circ$ and 180° for $\mu_0 H \geq 1$ T [15]. This suggests an increase in interlayer scattering for $\mathbf{H} \parallel \mathbf{a}$. However, similar to our discussion for EuMnBi_2 , the microscopic contributions of the magnetic order to the increase in scattering need to be further elucidated. Unlike EuMnBi_2 , quantum oscillations for EuMnSb_2 have not been seen for either M data taken down to 1.8 K and in fields up to 7 T or for ρ_{xx} data taken down to 2 K and in fields up to 13 T [15]. This is despite ARPES results for the **kl** plane at ≈ 20 K indicating Dirac-like linear bands near E_F [15].

Finally, quantum oscillations have been observed for tetragonal SrMnSb_2 and $\text{Sr}_{1-x}\text{K}_x\text{MnSb}_2$, which have a C-type AFM structure of the Mn moments below $T_N \approx 300$ K [11, 12], similar to what we find for the Mn sublattice in EuMnSb_2 . ARPES data for SrMnSb_2 are consistent with the size of the Fermi-surface pockets determined from the quantum oscillations [34]. However, DFT and tight-binding calculations find that the Dirac-cone nodes are $\approx 200\text{--}300$ meV above E_F [34, 35]. The presence of vacancies at the Sr and Mn crystallographic sites (i.e. $\text{Sr}_{1-y}\text{Mn}_{1-z}\text{Sb}_2$) have been shown to affect the electronic-band structure [11, 36], potentially shifting E_F towards the Dirac nodes [35]. Thus, these results further question the structural and magnetic properties necessary for tunable topological properties.

Total energy and DFT calculations have shown that the square geometry of the Sb in SrMnSb_2 and the Bi in EuMnBi_2 in the X_2 layers are more amenable to the occurrence of topological fermions than the zigzag chain of the Sb in the X_2 layers in EuMnSb_2 [18, 37, 38]. On the other hand, it is also recognized that the details of any magnetic order can also play a role in tuning topological properties [37, 38], and our results detailing the various AFM states are important inputs for

future calculations. In particular DFT calculations and complementary ARPES measurements for the $T < T_{\text{N}_{\text{Eu2}}}$ phase of EuMnSb_2 should be enlightening.

V. CONCLUSION

We have presented a detailed study of the magnetic structures present in the zero-field AFM phases of EuMnSb_2 . In addition to the two higher- T phases already observed in some single-crystal studies, we observe a third AFM phase below $T_{\text{N}_{\text{Eu2}}} = 9(1)$ K. To summarize, we find that upon cooling below $T_{\text{N}_{\text{Mn}}} = 323(1)$ K, the Mn magnetic sublattice orders into the C-type AFM structure shown in Fig. 1(e), with $\mu_{\text{Mn}} = 3.0(2) \mu_B$ lying along **a** at $T = 50$ K. Below $T_{\text{N}_{\text{Eu1}}} = 23(1)$ K, the Eu lattice orders as shown in Fig. 1(f) with μ_{Eu} canted in the **ac** plane. At 12 K, $\mu_{\text{Eu}} = 4.7(2) \mu_B$ and $\phi_{\text{ac}} = 31(1)^\circ$. Finally, below $T_{\text{N}_{\text{Eu2}}}$, μ_{Eu} develops a large component along **b**, and $\mu_{\text{Eu}} = 5.6(4) \mu_B$ with components of $2.4(4)$, $4.3(2)$, and $2.6(2) \mu_B$ lying along **a**, **b**, and **c**, respectively, at 5 K. This structure is shown in Fig. 1(g). The presence of short-range magnetic correlations between $12 \text{ K} \lesssim T \lesssim 30 \text{ K}$ is additionally indicated by the Mössbauer, neutron diffraction, and $C_p(T)$ data. Using these results, we have postulated the signs of NN intraplane and interplane exchange and magnetic anisotropy present within a general Heisenberg-model description of the magnetism. The signs of these interactions should provide vital input for DFT and other calculations.

We also have discussed how the discovery of magnetic order producing a net magnetization which in turn gives rise to an effective magnetic field across the Sb2 layers would be a highly desirable result. Whereas we do not find that this is the case for any of the three AFM states, the discovery of multiple AFM transitions with differing orientations of μ_{Eu} points to competition between different states and may lead to useful tunability of the magnetism and, in turn, insight into magnetically tuning topological properties in related compounds. New DFT and total energy calculations incorporating our detailed description for the various AFM states as well as systematic studies subtly varying the amount of disorder in EuMnSb_2 should give enlightening results concerning the topological tunability of AMnX_2 compounds.

ACKNOWLEDGMENTS

We are grateful for J. Schmidt's assistance with the EDS measurements and appreciate assistance and advice from D. Vaknin. This research was supported by the Center for Advancement of Topological Semimetals, an Energy Frontier Research Center funded by the U.S. Department of Energy Office of Science, Office of Basic Energy Sciences, through the Ames Laboratory under Contract No. DE-AC02-07CH11358. The research was primarily performed at the Ames Laboratory which is operated for the U.S. Department of Energy by Iowa State University under Contract No. DE-AC02-07CH11358. JMW, YL, SLB, and AK were supported by Field Work Proposals at the Ames Laboratory. A portion of

this research used resources at the Spallation Neutron Source, a U. S. DOE Office of Science User Facility operated by the Oak Ridge National Laboratory. Financial support for this work was provided by Fonds Québécois de la Recherche sur la Nature et les Technologies, and the Natural Sciences and

Engineering Research Council (NSERC) Canada. Much of this work was carried out while DHR was on sabbatical at Iowa State University and their generous support during this visit is gratefully acknowledged.

-
- [1] M. Z. Hasan and C. L. Kane, Colloquium: topological insulators, *Rev. Mod. Phys.* **82**, 3045 (2010).
- [2] A. Bansil, H. Lin, and T. Das, Colloquium: Topological band theory, *Rev. Mod. Phys.* **88**, 021004 (2016).
- [3] N. Armitage, E. Mele, and A. Vishwanath, Weyl and Dirac semimetals in three-dimensional solids, *Rev. Mod. Phys.* **90**, 015001 (2018).
- [4] D. Vanderbilt, *Berry Phases in Electronic Structure Theory: Electric Polarization, Orbital Magnetization and Topological Insulators* (Cambridge University Press, 2018).
- [5] B. Lv, T. Qian, and H. Ding, Experimental perspective on three-dimensional topological semimetals, *Rev. Mod. Phys.* **93**, 025002 (2021).
- [6] S. X. M. Riberolles, T. V. Trevisan, B. Kuthanazhi, T. W. Heitmann, F. Ye, D. C. Johnston, S. L. Bud'ko, D. H. Ryan, P. C. Canfield, A. Kreyssig, A. Vishwanath, R. J. McQueeney, L. L. Wang, P. P. Orth, and B. G. Ueland, Magnetic crystalline-symmetry-protected axion electrodynamics and field-tunable unpinned Dirac cones in EuIn_2As_2 , *Nat. Commun.* **12**, 999 (2021).
- [7] J.-R. Soh, S. M. Tobin, H. Su, I. Zivkovic, B. Ouladdiaf, A. Stunault, J. A. Rodríguez-Velamazán, K. Beauvois, Y. Guo, and A. T. Boothroyd, Magnetic structure of the topological semimetal YbMnSb_2 , *Phys. Rev. B* **104**, L161103 (2021).
- [8] B. Q. Lv, H. M. Weng, B. B. Fu, X. P. Wang, H. Miao, J. Ma, P. Richard, X. C. Huang, L. X. Zhao, G. F. Chen, Z. Fang, X. Dai, T. Qian, and H. Ding, Experimental Discovery of Weyl Semimetal TaAs, *Phys. Rev. X* **5**, 031013 (2015).
- [9] S.-Y. Xu, N. Alidoust, I. Belopolski, Z. Yuan, G. Bian, T.-R. Chang, H. Zheng, V. N. Strocov, D. S. Sanchez, G. Chang, *et al.*, Discovery of a Weyl fermion state with Fermi arcs in niobium arsenide, *Nat. Phys.* **11**, 748 (2015).
- [10] Y. Feng, Z. Wang, C. Chen, Y. Shi, Z. Xie, H. Yi, A. Liang, S. He, J. He, Y. Peng, X. Liu, Y. Liu, L. Zhao, G. Liu, X. Dong, J. Zhang, C. Chen, Z. Xu, X. Dai, Z. Fang, and X. J. Zhou, Strong Anisotropy of Dirac Cones in SrMnBi_2 and CaMnBi_2 Revealed by Angle-Resolved Photoemission Spectroscopy, *Sci. Rep.* **4**, 5385 (2014).
- [11] J. Y. Liu, J. Hu, Q. Zhang, D. Graf, H. B. Cao, S. M. A. Radmanesh, D. J. Adams, Y. L. Zhu, G. F. Cheng, X. Liu, W. A. Phelan, J. Wei, M. Jaime, F. Balakirev, D. A. Tennant, J. F. DiTusa, I. Chiorescu, L. Spinu, and Z. Q. Mao, A magnetic topological semimetal $\text{Sr}_{1-y}\text{Mn}_{1-z}\text{Sb}_2$ ($y, z < 0.1$), *Nat. Mater.* **16**, 905 (2017).
- [12] Y. Liu, T. Ma, L. Zhou, W. E. Straszheim, F. Islam, B. A. Jensen, W. Tian, T. Heitmann, R. A. Rosenberg, J. M. Wilde, B. Li, A. Kreyssig, A. I. Goldman, B. G. Ueland, R. J. McQueeney, and D. Vaknin, Crystal growth, microstructure, and physical properties of SrMnSb_2 , *Phys. Rev. B* **99**, 054435 (2019).
- [13] K. Momma and F. Izumi, *J. Appl. Crystallogr.* **44**, 1272 (2011).
- [14] H. Masuda, H. Sakai, M. Tokunaga, Y. Yamasaki, A. Miyake, J. Shiojai, S. Nakamura, S. Awaji, A. Tsukazaki, H. Nakao, *et al.*, Quantum Hall effect in a bulk antiferromagnet EuMnBi_2 with magnetically confined two-dimensional Dirac fermions, *Sci. Adv.* **2**, e1501117 (2016).
- [15] J.-R. Soh, P. Manuel, N. Schröter, C. Yi, F. Orlandi, Y. Shi, D. Prabhakaran, and A. Boothroyd, Magnetic and electronic structure of Dirac semimetal candidate EuMnSb_2 , *Phys. Rev. B* **100**, 174406 (2019).
- [16] D. Gong, S. Huang, F. Ye, X. Gui, J. Zhang, W. Xie, and R. Jin, Canted Eu magnetic structure in EuMnSb_2 , *Phys. Rev. B* **101**, 224422 (2020).
- [17] Q. Zhang, J. Liu, H. Cao, A. Phelan, D. Graf, J. F. DiTusa, D. A. Tennant, and Z. Mao, Toward tunable quantum transport and novel magnetic states in $\text{Eu}_{1-x}\text{Sr}_x\text{Mn}_{1-z}\text{Sb}_2$ ($z < 0.05$), *NPG Asia Mater.* **14**, 22 (2022).
- [18] C. Yi, S. Yang, M. Yang, L. Wang, Y. Matsushita, S. Miao, Y. Jiao, J. Cheng, Y. Li, K. Yamaura, Y. Shi, and J. Luo, Large negative magnetoresistance of a nearly Dirac material: Layered antimonide EuMnSb_2 , *Phys. Rev. B* **96**, 205103 (2017).
- [19] C. Voyer and D. Ryan, A complete solution to the Mössbauer problem, all in one place, *Hyperfine Interactions* **170**, 91 (2006).
- [20] P. Bonville, J. Hodges, M. Shirakawa, M. Kasaya, and D. Schmitt, Incommensurate modulated magnetic structure in orthorhombic EuPdSb , *The European Physical Journal B-Condensed Matter and Complex Systems* **21**, 349 (2001).
- [21] A. Maurya, P. Bonville, A. Thamizhavel, and S. Dhar, EuNiGe_3 , an anisotropic antiferromagnet, *Journal of Physics: Condensed Matter* **26**, 216001 (2014).
- [22] N. Qureshi, MAG2POL: A program for the analysis of spherical neutron polarimetry, flipping ratio and integrated intensity data, *J. Appl. Crystallogr.* **52**, 175 (2019).
- [23] L. Coates, H. B. Cao, B. C. Chakoumakos, M. D. Frontzek, C. Hoffmann, A. Y. Kovalevsky, Y. Liu, F. Meilleur, A. M. dos Santos, D. A. A. Myles, X. P. Wang, and F. Ye, A suite-level review of the neutron single-crystal diffraction instruments at Oak Ridge National Laboratory, *Rev. Sci. Instrum.* **89**, 092802 (2018).
- [24] A. J. Schultz, K. Srinivasan, R. G. Teller, J. M. Williams, and C. Lukehart, Single-crystal, time-of-flight, neutron-diffraction structure of hydrogen *cis*-diacetyltetracarboxylrheneate, $[\text{cis}-(\text{OC})_4\text{Re}(\text{CH}_3\text{CO})_2] \text{H}$: a metallaacetylacetonate molecule, *J. Am. Chem. Soc.* **106**, 999 (1984).
- [25] M. Dušek, V. Petříček, M. Wunschel, R. Dinnebier, and S. v. Smaalen, Refinement of modulated structures against X-ray powder diffraction data with JANA2000, *J. Appl. Crystallogr.* **34**, 398 (2001).
- [26] D. Ryan, A. Legros, O. Niehaus, R. Pöttgen, J. Cadogan, and R. Flacau, Modulated ferromagnetic ordering and the magnetocaloric response of Eu_4PdMg , *Journal of Applied Physics* **117**, 17D108 (2015).
- [27] N. S. Sangeetha, S. Pakhira, D. H. Ryan, V. Smetana, A.-V. Mudring, and D. C. Johnston, Magnetic phase transitions in $\text{Eu}(\text{Co}_{1-x}\text{Ni}_x)_2\text{As}_2$ single crystals, *Phys. Rev. Mater.* **4**, 084407 (2020).
- [28] H. T. Stokes, D. M. Hatch, and B. J. Campbell, ISODISTORT, ISOTROPY Software Suite, iso.byu.edu.

- [29] B. J. Campbell, H. T. Stokes, D. E. Tanner, and D. M. Hatch, ISODISPLACE: a web-based tool for exploring structural distortions, *J. Appl. Crystallogr.* **39**, 607 (2006).
- [30] T. Chattopadhyay, H. G. Schnering, and P. J. Brown, Neutron diffraction study of the magnetic ordering in EuAs_3 , *J. Magn.* **28**, 247 (1982).
- [31] A. F. May, M. A. McGuire, and B. C. Sales, Effect of Eu magnetism on the electronic properties of the candidate Dirac material EuMnBi_2 , *Phys. Rev. B* **90**, 075109 (2014).
- [32] H. Masuda, H. Sakai, M. Tokunaga, M. Ochi, H. Takahashi, K. Akiba, A. Miyake, K. Kuroki, Y. Tokura, and S. Ishiwata, Impact of antiferromagnetic order on Landau-level splitting of quasi-two-dimensional Dirac fermions in EuMnBi_2 , *Phys. Rev. B* **98**, 161108 (2018).
- [33] H. Masuda, H. Sakai, H. Takahashi, Y. Yamasaki, A. Nakao, T. Moyoshi, H. Nakao, Y. Murakami, T. Arima, and S. Ishiwata, Field-induced spin reorientation in the antiferromagnetic Dirac material EuMnBi_2 revealed by neutron and resonant x-ray diffraction, *Phys. Rev. B* **101**, 174411 (2020).
- [34] S. V. Ramankutty, J. Henke, A. Schiphorst, R. Nutakki, S. Bron, G. Araizi-Kanoutas, S. K. Mishra, L. Li, Y. K. Huang, T. K. Kim, M. Hoesch, C. Schlueter, T. L. Lee, A. de Visser, Z. Zhong, J. van Wezel, E. van Heumen, and M. S. Golden, Electronic structure of the candidate 2D Dirac semimetal SrMnSb_2 : a combined experimental and theoretical study, *SciPost Phys.* **4**, 010 (2018).
- [35] Q. Zhang, S. Okamoto, M. B. Stone, J. Liu, Y. Zhu, J. DiTusa, Z. Mao, and D. A. Tennant, Influence of magnetism on Dirac semimetallic behavior in nonstoichiometric $\text{Sr}_{1-y}\text{Mn}_{1-z}\text{Sb}_2$ ($y \sim 0.07$, $z \sim 0.02$), *Phys. Rev. B* **100**, 205105 (2019).
- [36] A. Saadi, L. Omari, A. Lekdadri, H. Lassri, and A. Boudali, Effect of a small Mn and Sr deficiency on the physical properties of SrMnSb_2 , *Mater. Today: Proc.* **37**, 3821 (2021), 2019.
- [37] G. Lee, M. A. Farhan, J. S. Kim, and J. H. Shim, Anisotropic Dirac electronic structures of AMnBi_2 ($A = \text{Sr, Ca}$), *Phys. Rev. B* **87**, 245104 (2013).
- [38] M. A. Farhan, G. Lee, and J. H. Shim, AEMnSb_2 ($\text{AE} = \text{Sr, Ba}$): a new class of Dirac materials, *J. Phys. Condens. Matter.* **26**, 042201 (2014).